

This is the accepted manuscript made available via CHORUS. The article has been published as:

## Atomistic mechanisms of the initial oxidation of stepped math

$\text{Cu}_3\text{Au}$   
 $(100)$

Yaguang Zhu, Dongxiang Wu, Chaoran Li, Xiao Tong, J. Anibal Boscoboinik, Jerzy T. Sadowski, and Guangwen Zhou

Phys. Rev. B **105**, 075422 — Published 22 February 2022

DOI: [10.1103/PhysRevB.105.075422](https://doi.org/10.1103/PhysRevB.105.075422)

# Atomistic mechanisms of the initial oxidation of stepped Cu<sub>3</sub>Au(100)

Yaguang Zhu<sup>1</sup>, Dongxiang Wu<sup>1</sup>, Chaoran Li<sup>1</sup>, Xiao Tong<sup>2</sup>, J. Anibal Boscoboinik<sup>2</sup>,  
Jerzy T. Sadowski<sup>2</sup>, Guangwen Zhou<sup>1\*</sup>

<sup>1</sup>Department of Mechanical Engineering & Materials Science and Engineering Program, State  
University of New York, Binghamton, NY 13902, USA

<sup>2</sup>Center for Functional Nanomaterials, Brookhaven National Laboratory, Upton, New York 11973

## Abstract

---

Alloy oxidation is complex and involves several critical processes that lack of understanding on the atomic level. Here we report an atomistic picture of the initial-stage oxidation of stepped Cu<sub>3</sub>Au(100) using a combination of surface science tools and modeling to illuminate the microscopic processes underlying oxygen-adsorption induced structural and compositional changes. The pristine Cu<sub>3</sub>Au(100) consists of wide CuAu-terminated terraces and narrow Cu-terminated terraces separated by monatomic steps. Counterintuitive to the common expectations of the adsorbate-induced surface segregation of the more reactive alloy component, our observations demonstrate that the oxygen adsorption leads to the exfoliation of the outermost CuAu layer, thereby exposing the inner Cu plane to O attack. This occurs via the oxygen-assisted abstraction of Au and Cu atoms from step edges and CuAu terraces, which generates a large number of Cu adatoms aggregating into Cu clusters and Au adatoms dissolving into the bulk. The oxygen adsorption onto four-fold hollow sites of the exposed Cu plane results in nucleation and growth of the c(2×2)-O superstructure, which can be fit well by the Johnson–Mehl–Avrami–Kolmogorov theory with a site-saturate nucleation mechanism.

---

\*To whom correspondence should be addressed: [gzhou@binghamton.edu](mailto:gzhou@binghamton.edu)

## 1        **1. Introduction**

2        Oxidation is a degradation phenomenon of a metallic material resulting from chemical  
3 reactions in which the metal combines with oxygen to form oxides. It is ubiquitous because most  
4 metals are reactive in their functioning environments and have a strong driving force to transform  
5 to their low-energy oxide state. Alloying is often used to modify material properties with respect  
6 to pure metals. One classic example of alloying is the development of alloys with enhanced  
7 oxidation resistance resulting from the formation of a stable and protective oxide layer. Despite  
8 its seeming simplicity, oxidation is a rather complicated process because it covers many fields of  
9 materials science, ranging from basic thermodynamics of gas-surface reactions, defect chemistry,  
10 surface/interface, bulk and short-circuit diffusion and phase transformations to interface-reaction  
11 induced stress generation and relaxation, many of which are coupled and involved from the onset  
12 of the reaction. Much of our current knowledge of oxidation is derived from the work based on the  
13 growth of macroscopically thick oxide that is too coarse to reflect the microscopic details of the  
14 early-stage oxidation. Microscopic atomic-scale observations of alloy oxidation are still rare but  
15 are essential for developing a fundamental understanding of the environmental stability and  
16 functionality of alloys. Compared to the oxidation of pure metals, alloy oxidation is generally much  
17 more complex. The possible effects of alloying on the oxidation process include different oxygen  
18 affinities of the alloying elements, formation of multiple oxides and solid solubility between them,  
19 and different mobilities of various metal ions in the alloy and the oxides. A detailed understanding  
20 of the key processes taking place in the critical early stages of the oxidation is even more  
21 challenging because of the overwhelming presence of structural defects at the surface and the  
22 difficulty of atomically probing the complex interplay among oxygen atoms, alloying elements and  
23 structural defects.

1        Herein we address the early-stage oxidation of  $\text{Cu}_3\text{Au}(100)$  with the use of a combination of  
2 scanning tunneling microscopy (STM) imaging, low-energy electron diffraction (LEED), low-  
3 energy ion scattering (LEIS), and synchrotron-based ambient-pressure X-ray photoelectron  
4 spectroscopy (AP-XPS) to provide complementary information on surface structure, composition,  
5 and chemistry in conjunction with atomistic modeling. The  $\text{Cu}_3\text{Au}(100)$  surface examined in our  
6 study consists of a series of monatomic atomic steps alternating with flat terraces, a characteristic  
7 morphology common to most crystal surfaces. We seek the effects of alloying and atomic steps  
8 on oxygen-adsorption induced compositional and structural transformation at the alloy surface.  
9 The Cu-Au system is considered for both its fundamental and practical importance.  
10 Fundamentally, the dramatic difference in the oxygen affinity between Cu and Au atoms allows  
11 some of the features of the early-stage alloy oxidation to be examined without the complication of  
12 competing oxygen adsorption by reactive alloying elements. Practically, bimetallic Cu-Au alloys  
13 show improved reactivity over the single metal counterparts [1] for various catalytic oxidation  
14 reactions including CO oxidation [2,3],  $\text{CO}_2$  reduction [4,5], methanol production [6,7], and the  
15 water-gas shift reaction [8,9]. These catalytic reactions are initiated from the adsorption and  
16 dissociation of oxygen-containing species, which depend on surface structure, composition, and  
17 coordination environment around defective sites. A proper interpretation of the catalytic properties  
18 of Cu-Au alloys requires a precise knowledge of the surface composition and structural  
19 transformation induced by oxygen adsorption. A  $\text{Cu}_3\text{Au}$  surface can be a model system for  
20 establishing the fundamental principles to control the adsorption properties of alloys by tuning the  
21 segregation and desegregation of the alloying elements with the chemical stimuli.

22

## 23        **2. Experimental and Computational Details**

1 A Cu<sub>3</sub>Au(100) single crystal (Princeton Scientific Corp.) was used for the oxidation  
2 experiments. The Cu<sub>3</sub>Au(100) was cut to within 0.1° to the (100) crystallographic orientation and  
3 polished to a mirror finish. A clean surface can be achieved by repeated cycles of Ar<sup>+</sup> sputtering  
4 at room temperature ( $2 \times 10^{-5}$  Torr of Ar<sup>+</sup>,  $8 \mu\text{A cm}^{-2}$ , 1.5 keV) and ultrahigh vacuum (UHV)  
5 annealing at 600 °C for 10 min. The STM experiments were performed with an UHV system  
6 consisting of a sample preparation chamber (base pressure  $\sim 1 \times 10^{-10}$  Torr) for the surface  
7 preparation and an STM chamber (base pressure  $\sim 1 \times 10^{-11}$  Torr) for surface imaging. Surface  
8 cleanliness and order were checked by STM, LEED and XPS. Oxidation was performed by  
9 exposing the clean surface to high-purity (99.9999%) oxygen gas at an oxygen partial pressure  
10 ( $p_{\text{O}_2}$ ) of  $1 \times 10^{-6}$  Torr and 350 °C. The STM imaging was performed at room temperature with an  
11 electrochemically etched tungsten tip and the bias was applied on the sample. Separate UHV  
12 systems equipped with LEED and LEIS with a SPECS Phoibos 100 energy analyzer were used  
13 to further confirm the crystal structure and surface composition of the Cu<sub>3</sub>Au(100) prepared using  
14 the similar procedure as that in the STM measurements.

15 AP-XPS was employed to monitor the surface composition and chemistry evolution of the  
16 Cu<sub>3</sub>Au(100) as a function of the O<sub>2</sub> exposure at  $p_{\text{O}_2} = 1 \times 10^{-6}$  Torr and 350 °C. The AP-XPS  
17 experiments were performed at the IOS beamline of the National Synchrotron Light Source II  
18 (NSLS-II), Brookhaven National Laboratory. The detailed instrument setup can be found from  
19 previous work [10–13]. In short, the multiple differential pumping stages between the main  
20 chamber and the hemispherical analyzer allow for eliminating the scattering effect of gas  
21 molecules and continuously acquiring XPS spectra in the presence of gas at the pressure of  $1 \times 10^{-6}$   
22 Torr. The photon energy range of the beamline is from 250 to 2000 eV, which covers O 1s, Cu  
23 2p, Cu 3p, Au 4f core levels and Cu LMM relevant for the present work. Real-time monitoring of  
24 the surface composition evolution induced by surface segregation was performed by acquiring

1 spectra of the Au 4f core level *in situ*. All spectra were collected at a takeoff angle of 20° between  
2 the sample surface and the electron analyzer optics of the XPS spectrometer. Binding energies  
3 in each spectrum were referred to the Fermi level for correction and XPS spectra were analyzed  
4 with the Voigt lineshape and Shirley-type background. Line shape of a Gaussian/Lorentzian sum  
5 formula modified using an exponential tail function was introduced for accurate peak fitting and  
6 deconvolution. Full width at half-maximum (FWHM) of Au was 0.5-0.6 eV for alloy Au and 0.4-0.5  
7 eV for metallic Au. Integrated peak areas of each Au species were used to calculate the relative  
8 composition evolution.

9 The density functional theory (DFT) calculations made use of the Vienna ab initio simulation  
10 package (VASP), employing plane-wave functionals with the projector augmented wave  
11 approach [14–17]. The generalized gradient approximation (GGA) with the Perdew-Burke-  
12 Ernzerhof (PBE) exchange-correlation functional was used to evaluate the exchange-correlation  
13 energy [18,19]. Our computational framework is similar to previous work [20]. The plane wave  
14 energy cut-off energy was set as 400 eV. Monkhorst-Pack k-point grids of 4×4×1 and 4×2×1 were  
15 used for the CuAu surface calculations [21]. We used period slabs with a vacuum spacing of 12  
16 Å to model the surface, and the slab is composed of 5 layers with the bottom two layers fixed. All  
17 the structures were fully relaxed until the force acting on each atom was lower than 0.015 eV/Å.  
18 The Cu<sub>3</sub>Au(100) surface is known to ripple with the Au atoms being displaced above the Cu atoms.  
19 The magnitude of the rippling found experimentally (~0.12 Å [22], ~0.04 Å [23]) and theoretically  
20 (~0.18 Å [24], ~0.15 Å [25]) is reasonably reproduced in our DFT calculations (~0.26 Å). Our DFT  
21 calculations of the O adsorption at Cu<sub>3</sub>Au(100) are based on the fully relaxed Cu<sub>3</sub>Au(100), for  
22 which the surface ripping effect is incorporated.

23 We investigated the vacancy formation energy of Cu and Au in our DFT modeling to explore  
24 the surface structure evolution. The most stable configuration identified after

1 removing a Cu or Au atom was used as a starting configuration for the next atom removal. The  
2 vacancy formation energy was computed using the equation

$$3 \quad E_{vac} = E_{slab}^{tot} - E_{ref} - E_{atom}, \quad (1)$$

4 where  $E_{slab}^{tot}$  is the total energy of the whole CuAu system;  $E_{ref}$  is the free energy of the slab with  
5 one Cu or Au vacancy,  $E_{atom}$  is the free energy of single Cu/Au atom in the bulk structure. All the  
6 atomic structures were visualized using the Visualization for Electronic and Structure Analysis  
7 (VESTA).

8

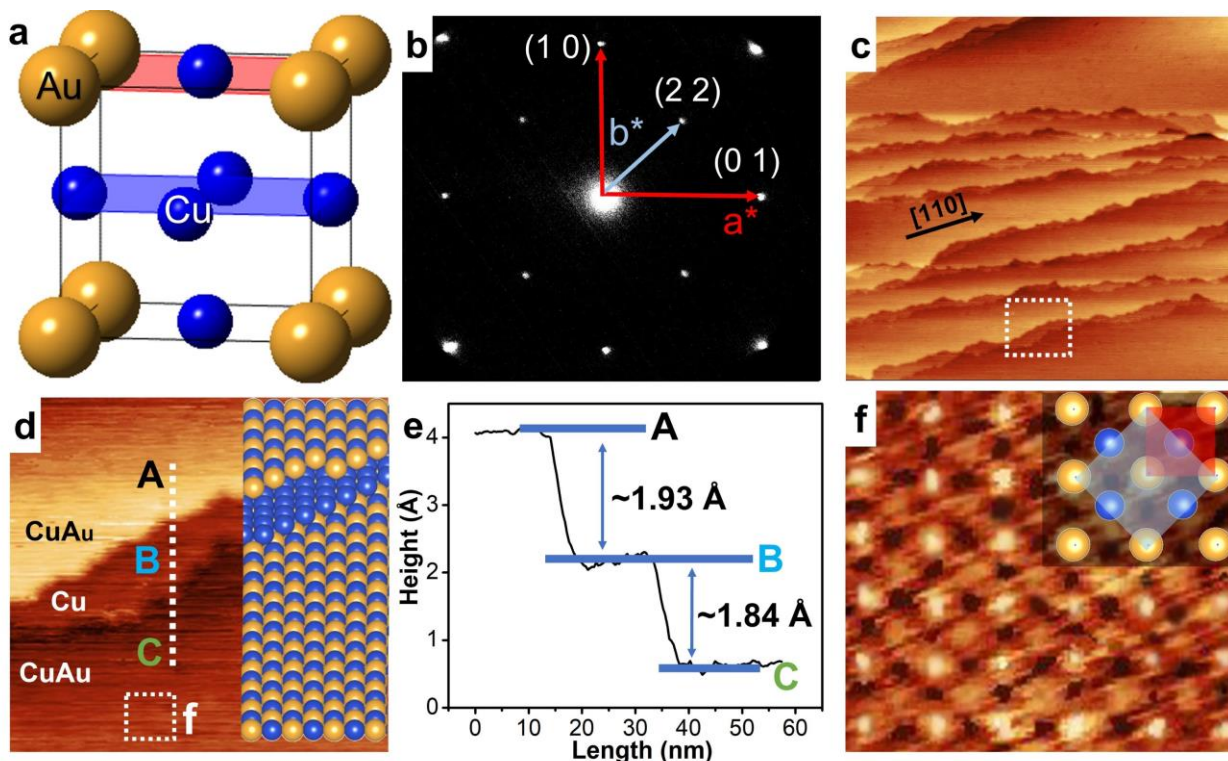
### 9 **3. Results**

#### 10 **3.1 STM imaging**

11  $\text{Cu}_3\text{Au}$  has a cubic,  $L1_2$  ordered structure and transforms to a substitutionally disordered  
12 face-center cubic (fcc) lattice on heating over the bulk order-disorder transition temperature of ~  
13 390 °C. In  $L1_2$  ordered  $\text{Cu}_3\text{Au}$ , Au atoms occupy the corners of the fcc unit cell and Cu the face  
14 centers (Fig. 1(a)). Therefore, the ordered  $\text{Cu}_3\text{Au}(100)$  surface could be terminated in a plane of  
15 (i) pure Cu (i.e., CuCu plane) or (ii) in a plane consisting of equal numbers of Cu and Au atoms  
16 (CuAu plane) [26]. Fig. 1(b) shows a LEED pattern of the  $\text{Cu}_3\text{Au}(100)$  crystal that was annealed  
17 at 350 °C in UHV to restore the chemical order of the alloy. The LEED pattern reveals a  $p(1 \times 1)$   
18 symmetry and a clear  $c(2 \times 2)$  superstructure, as marked in Fig. 1(b). The  $c(2 \times 2)$  superstructure is  
19 due to the  $L1_2$ -ordered lattice and suggests the CuAu surface termination. Fig. 1(c) displays a  
20 representative STM topographic image of the  $\text{Cu}_3\text{Au}(100)$  surface, showing that the well-  
21 annealed surface consists of alternating wide and narrow terraces separated by atomic steps that  
22 exhibit a sawtooth-like, zigzag appearance with the preferred terrace edge orientation along the  
23  $[110]$  direction. Fig. 1(d) presents a zoomed-in STM image of the stepped region as marked by

1 the white dashed box in Fig. 1(c), showing that the atomic steps consist of a wide terrace ( $\geq 50$   
2 nm) and a narrow terrace ( $\sim 5-10$  nm). As illustrated schematically in the inset of Fig. 1(d) and  
3 confirmed later by the step height profile and atomically resolved STM imaging analysis, the wide  
4 terraces are terminated by the CuAu plane whereas the narrow terraces have the surface  
5 termination of the pure Cu plane. Fig. 1(e) displays the STM height profile along the white dashed  
6 line in Fig. 1(d), showing a step height of  $\sim 1.93$  Å between the upper CuAu(100)-terminated  
7 terrace (A) and the lower Cu(100)-terminated terrace (B), but a slightly smaller step height of  $\sim$   
8  $1.84$  Å between the Cu(100)-terminated terrace (B) and the bottom CuAu(100)-terminated terrace  
9 (C). This slight differences in the step heights can be attributed to the upward relaxation of Au  
10 atoms in the CuAu terminated surface of  $L1_2$  ordered  $Cu_3Au(100)$ . [24] Since the  $L1_2$  ordered  
11  $Cu_3Au$  has a lattice constant of  $\sim 3.75$  Å [27,28], the measured step heights correspond to  
12 monoatomic steps. The surface terraces separated by monoatomic steps should have different  
13 chemical configurations, i.e., the surface planes of CuAu and pure Cu, as highlighted in the inset  
14 of Fig. 1(d).

15



1  
 2 **Fig. 1:** (a) The crystal model of  $L1_2$  ordered  $\text{Cu}_3\text{Au}$ . The possible surface terminations in a plane  $\text{CuAu}$  or  
 3 pure  $\text{Cu}$  are marked in purple and blue, respectively. (b) LEED pattern of clean ordered  $\text{Cu}_3\text{Au}(100)$ , where  
 4 the  $(2, 2)$  spot corresponds to the superlattice cell shown in the inset of (f). Primary electron energy:  $E = 25$   
 5 eV. (c) Topographic STM image (size:  $500 \times 500 \text{ nm}^2$ ) of an ordered  $\text{Cu}_3\text{Au}(100)$  surface, showing that the  
 6 surface consists of wide and narrow terraces with a preferred terrace edge orientation along  $[011]$ . (d)  
 7 Zoomed-in STM image of the stepped region as marked by the white dashed box in (c) (size:  $40 \times 40 \text{ nm}^2$ ).  
 8 The inset shows schematically the surface termination of the wide and narrow terraces, gold and blue balls  
 9 represent  $\text{Au}$  and  $\text{Cu}$  atoms, respectively. (e) Surface profile along the white dashed line marked in (d),  
 10 indicating that the terraces are separated by monolayer atomic steps. (f) Atomically resolved STM image  
 11 of the wide terrace as marked by the white dashed square in (d) (size:  $2 \times 2 \text{ nm}^2$ ). The upper-right inset  
 12 shows schematically the  $c(2 \times 2)$  superstructure of the ordered  $\text{Cu}_3\text{Au}(100)$ . The tunneling conditions for the  
 13 STM imaging: (c)  $V_B = 2 \text{ V}$ ,  $I_T = 0.1 \text{ nA}$ , (d, f)  $V_B = 0.1 \text{ V}$ ,  $I_T = 1 \text{ nA}$ .  
 14

15 Fig. 1(f) shows an atomically resolved STM image from the wide terrace as marked by the  
 16 white dashed box in Fig. 1(d). Although it is challenging to chemically resolving  $\text{Cu}$  and  $\text{Au}$  atoms  
 17 by STM imaging, one can find that the surface consists of two types of atoms, where the bright  
 18 intensity ones have a larger surface height (by  $\sim 0.13 \text{ \AA}$ ) than the weak intensity ones and  
 19 correspond to  $\text{Au}$  whereas the weak intensity ones can be assigned as  $\text{Cu}$ . It is worth mentioning

1 that STM is sensitive to topography convoluted with the electronic density of states, but the good  
2 match of the surface height difference between the Au and Cu atoms measured here with other  
3 experimental tools (0.12 Å by ion scattering spectroscopy [22]) and modeling results (~0.18 Å [24],  
4 ~0.15 Å [25]) suggests that the STM image contrast in Fig. 1(f) is dominated by geometric rather  
5 electronic effects. The measured distance between adjacent bright (Au) atoms is ~3.7 Å, which is  
6 also consistent with the lattice constant of the Cu<sub>3</sub>Au unit cell. The upper-right inset in Fig. 1(f)  
7 shows schematically the arrangement of Au and Cu atoms in the CuAu terminated surface, in  
8 which the marked parameters of the p(1×1) and c(2×2) unit cells are related by  $b = \sqrt{2}a$  with the  
9 45° rotation angle of the two cells. This makes the Wood's notation of the surface structure of the  
10 c(2×2). Therefore, it can be determined that the wide terraces are terminated by the CuAu plane  
11 of the L1<sub>2</sub> ordered Cu<sub>3</sub>Au(100).

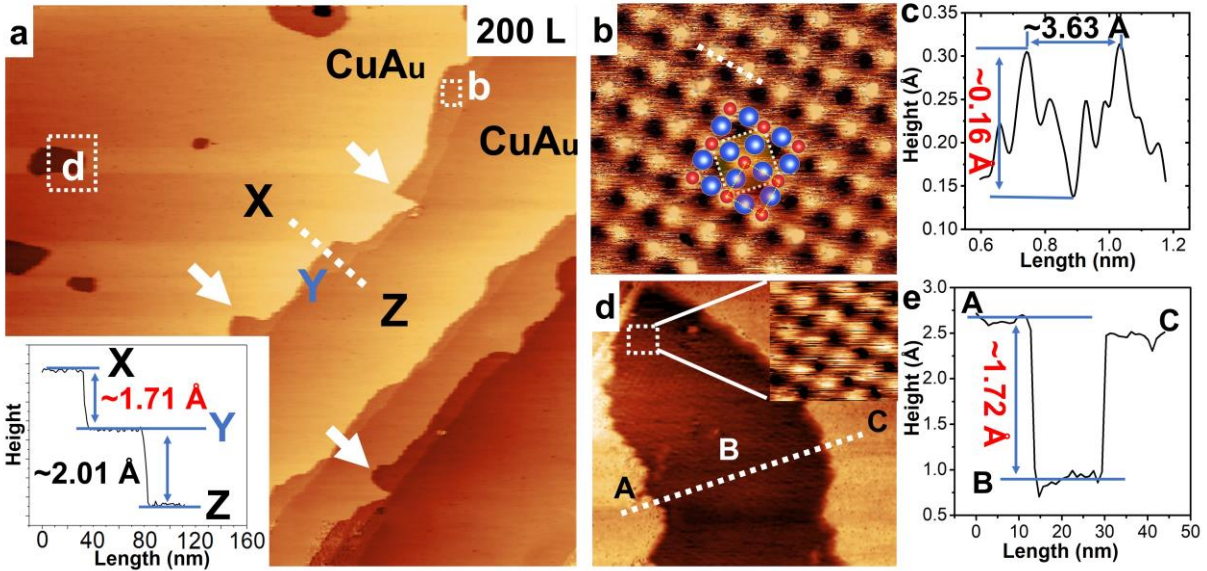
12 The above LEED and STM imaging demonstrate that the pristine surface prepared from  
13 the UHV annealing consists of alternating wide and narrow terraces separated by monoatomic  
14 steps, and the wide terrace terraces have the surface termination of the CuAu plane whereas the  
15 narrow terraces have the surface termination of the pure Cu plane. This provides the baseline to  
16 understand the onset of the surface oxidation and the resultant surface composition and structure  
17 evolution during the O<sub>2</sub> annealing. Fig. 2(a) shows a representative large-scale STM image of the  
18 Cu<sub>3</sub>Au(100) surface after 200 Langmuir (L) of O<sub>2</sub> exposure at 350 °C. The surface is still  
19 composed of wide (CuAu-terminated) and narrow (Cu-terminated) terraces, but the average  
20 extension of the narrow terraces is now of the order of ~ 15 nm, which is about a factor of 2 wider  
21 than that of the pristine surface (Fig. 1c). The widening of the narrow terraces is caused by the  
22 oxygen attack along the step edge of the wide terraces, which results in the receding motion of  
23 the step edges and the formation of local recessions into the wide terraces, as indicated by the  
24 white arrows in Fig. 2(a). As a result, the step edges become less zigzag with relatively long

1 straight segments because the protruding portion of the step edges is etched away first. In  
2 addition, the oxygen attack also takes place within the wide (CuAu) terraces, which results in the  
3 extraction of Au and Cu atoms from the topmost surface layer and leads to the formation of  
4 depressions (pits) in the terraces, as marked by white dashed box d in Fig. 2(a). The lower-left  
5 inset in Fig. 2(a) displays the STM height profile taken along the white dashed line across terraces  
6 X, Y and Z. Areas X and Z correspond to the wide, CuAu-terminated terraces that are separated  
7 by the narrow, Cu-terminated terrace (terrace Y). The line profile shows that a step height of ~  
8 1.71 Å between terraces X and Y, which is ~ 0.2 Å smaller than the step height (~ 1.9 Å) for the  
9 pristine surface (Figs. 1(d, e)). By contrast, the step height between terraces Y and Z is ~ 2.0 Å,  
10 a slight increase (by 0.2 Å) from the corresponding step height of the pristine surface (Figs. 1(d,  
11 e)).

12 Fig. 2(b) shows a zoomed-in STM image obtained from the Cu-terminated, narrow terrace,  
13 as marked by white dashed box b in Fig. 2(a). The atomically resolved STM image reveals a  
14  $c(2\times 2)$  structure of adsorbed oxygen, in which the oxygen atoms occupy the four-fold hollow sites  
15 of the Cu-terminated (100) terrace with 0.5 monolayer (ML) oxygen coverage, as shown  
16 schematically by the overlaid atomic structure in Fig. 2(b). The  $c(2\times 2)$ -O structure has been widely  
17 observed from oxygen adsorption on Cu(100) [14,29,30]. The  $c(2\times 2)$ -O formation observed here  
18 indicates that the Cu-terminated terraces of the  $L1_2$  ordered  $\text{Cu}_3\text{Au}(100)$  have the similar behavior  
19 in the oxygen adsorption on Cu(100). Fig. 2(c) displays the height profile along the white dashed  
20 line in Fig. 2(b), showing a lateral distance of 3.6 Å between the bright spots and a surface  
21 corrugation of ~0.2 Å. The measured distance equals to the distance between adjacent O atoms  
22 in  $c(2\times 2)$ -O, which indicates that the bright spots correspond to O atoms and the Cu atoms  
23 locating at the bridge sites of O atoms remain invisible in the STM image. This is also consistent  
24 with DFT calculations showing that the local density of states (LDOS) of O are higher than that of

1 Cu in  $c(2 \times 2)$ -O [31]. By comparison with the step heights for the pristine surface (Figs. 1(d, e)),  
 2 the O adsorption by the Cu-terminated terrace and the resultant upward relaxation of the surface  
 3 O atoms give rise to the decreased step height ( $\sim 1.71 \text{ \AA}$ ) between the lower Cu-terminated terrace  
 4 and the upper CuAu-terminated terrace but an increased step height ( $\sim 2.01 \text{ \AA}$ ) between the lower  
 5 CuAu-terminated terrace and the upper Cu-terminated terrace (the inset in Fig. 2(a)).

6 Fig. 2(d) shows a zoomed-in STM image obtained from the depression within the wide  
 7 terrace, as marked by white dashed box d in Fig. 2(a). The topographic STM image reveals that  
 8 the bottom surface of the depression displays the square-grid like structure, which is evident in  
 9 the inset zoomed-in STM image showing the same  $c(2 \times 2)$ -O structure as that in Fig. 2(b). This  
 10 suggests that it is a monolayer depression, and the bottom surface of the depression is terminated  
 11 by the Cu plane with adsorbed O at the four-fold hollow sites of Cu atoms. The monolayer  
 12 depression is further confirmed by the STM height profile taken along the white dashed line across  
 13 the depression in Fig. 2(d). As shown in Fig. 2(e), the depression has a depth of  $\sim 1.72 \text{ \AA}$ , which  
 14 matches well with the height of the monoatomic step between the lower oxygenated Cu terrace  
 15 and the upper CuAu terrace, as shown in the inset of Fig. 2(a).



1 **Fig. 2:** (a) Representative STM image (size:  $300 \times 300 \text{ nm}^2$ ) of the  $\text{Cu}_3\text{Au}(100)$  obtained after 200 L of  $\text{O}_2$   
2 exposure at  $350 \text{ }^\circ\text{C}$ . The lower-left inset is the surface profile along the white dashed line across the CuAu  
3 terraces (X, Z) and the narrow, Cu-terminated terrace (Y). (b) High-resolution STM image (size:  $2 \times 2 \text{ nm}^2$ )  
4 of the narrow terrace marked by white dashed box b in (a), in which only O atoms are visible. The  $c(2 \times 2)$ -  
5 O structure model is overlaid onto the STM image (the blue and red balls represent Cu and O atoms,  
6 respectively). (c) Surface profile along the white dashed line across two adjacent O atoms in (b). (d)  
7 Zoomed-in STM image (size:  $20 \times 20 \text{ nm}^2$ ) of the monolayer depression within the wide terrace marked  
8 with dashed box d in (a). The upper-right inset is an atomically resolved STM image (size:  $2 \times 2 \text{ nm}^2$ ) of the  
9 depression bottom marked with the dashed box. (e) Surface profile along the white dashed line across the  
10 terrace depression in (d). The tunneling conditions for STM imaging: (a)  $V_B = 2 \text{ V}$ ,  $I_T = 0.1 \text{ nA}$ , (b)  $V_B = 0.05$   
11  $\text{V}$ ,  $I_T = 1 \text{ nA}$ , and (d)  $V_B = 1.0 \text{ V}$ ,  $I_T = 0.1 \text{ nA}$ .

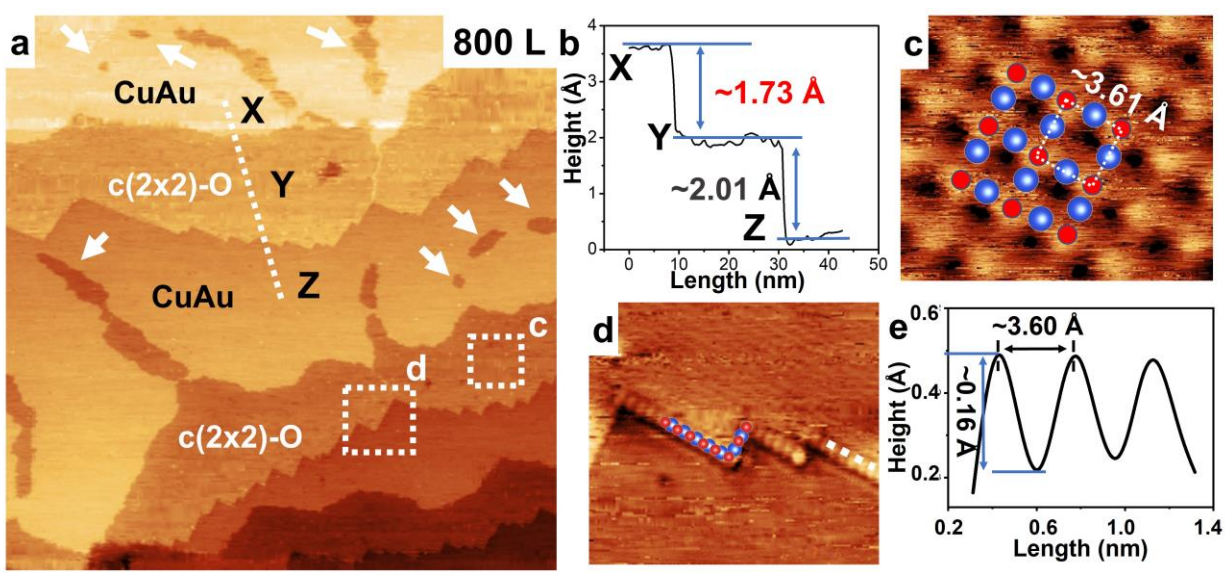
12

13 The above STM observations indicate that the  $\text{O}_2$  exposure results in O adsorption at the  
14 four-fold hollow sites of the Cu-terminated terraces. Meanwhile, the oxygen attack also leads to  
15 the decomposition of the topmost layer of the wide, CuAu terminated terraces via the formation  
16 of monolayer depressions and step-edge decay. To further confirm this trend, the evolution of the  
17 surface morphology and structure was monitored as a function of the  $\text{O}_2$  exposure at  $350 \text{ }^\circ\text{C}$  and  
18  $p_{\text{O}_2} = 1 \times 10^{-6} \text{ Torr}$ . Fig. 3(a) illustrates an STM image of the surface morphology after 800 L of  $\text{O}_2$   
19 exposure. The surface still consists of wide (CuAu-terminated) and narrow (Cu-terminated)  
20 terraces separated by monoatomic steps, as confirmed by the surface profile shown in Fig. 3(b).  
21 The average extension of the Cu terraces is of the order of  $\sim 30 \text{ nm}$ , about a factor of 3 larger  
22 than that of the pristine surface (Fig. 1c). The widening of the Cu terraces is caused by the step-  
23 edge decay of the CuAu terraces due to the continued oxygen attack along the step edge. As  
24 indicated by the white arrows in Fig. 3(a), the number density and size of depressions in the CuAu  
25 terminated terraces also increase upon the increased  $\text{O}_2$  exposure.

26 Fig. 3(b) shows the STM height profile taken along the white dashed line across terraces  
27 X, Y, and Z in Fig. 3(a). The step height of  $\sim 1.73 \text{ \AA}$  corresponds to the monoatomic step between  
28 the upper CuAu(100)-terminated terrace (X) and the lower Cu(100)-terminated,  $c(2 \times 2)$ -O terrace  
29 (Y), and the step height of  $\sim 2.01 \text{ \AA}$  is commensurate with the monoatomic step between the upper

1 Cu(100)- $c(2\times 2)$ -O terrace (Y) and the lower CuAu terrace (Z), consistent with the STM surface  
 2 profiles shown in Fig. 2. This is further confirmed by the atomically resolved STM image. As shown  
 3 in Fig. 3(c), the zoomed-in STM image of the region marked with white dashed box c in Fig. 3(a)  
 4 illustrates the  $c(2\times 2)$ -O superstructure formed on the Cu-terminated terrace. Fig. 3(d) is an  
 5 atomically resolved STM image of the stepped region, as marked with white dashed box d in Fig.  
 6 3(a), in which the bright dots can be assigned as O atoms because the STM image was obtained  
 7 using the same tunneling conditions as that for imaging the  $c(2\times 2)$ -O superstructure within the  
 8 terrace (Fig. 3(c)). The consideration of bright dots as O is further confirmed by the STM height  
 9 profile taken along the step edge across the bright dots in Fig. 3(d). As shown in Fig. 3(e), the  
 10 distance between the adjacent O atoms is  $\sim 3.60 \text{ \AA}$ , and the surface corrugation value is close to  
 11  $\sim 0.16 \text{ \AA}$ , which also matches that in the  $c(2\times 2)$ -O structure. Although the zigzag edges tend to be  
 12 defective and short, the STM observation reveals that O atoms are still adsorbed into the hollow  
 13 sites of the Cu atoms along the step edge region of the Cu-terminated terrace, as shown  
 14 schematically by the overlaid atomic structure in Fig. 3(d).

15



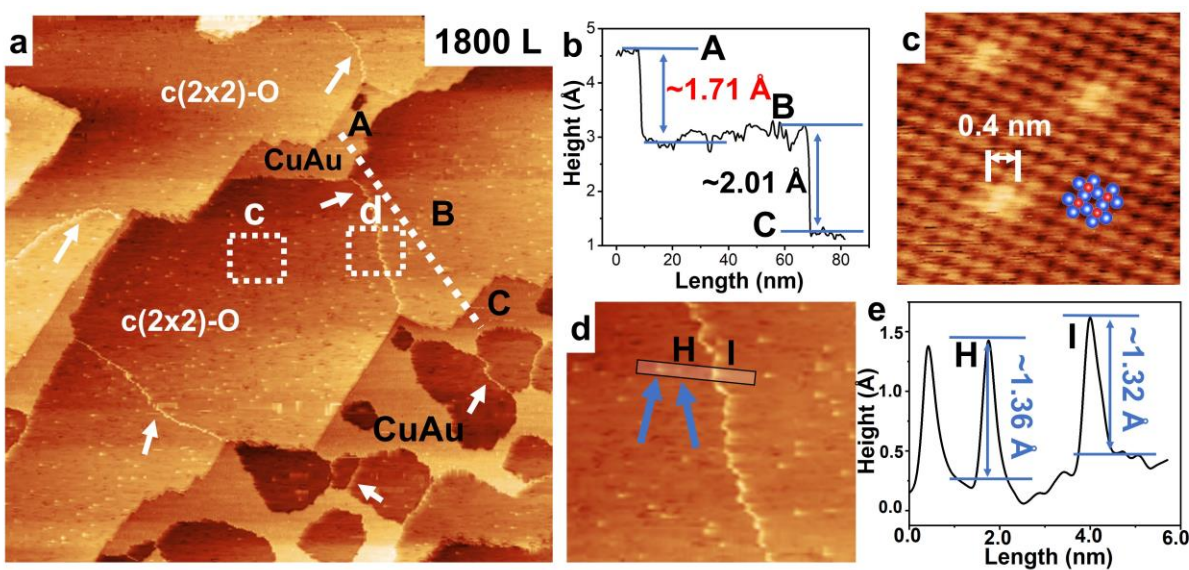
16

1 **Fig. 3:** (a) STM image (size:  $300 \times 300 \text{ nm}^2$ ) of the  $\text{Cu}_3\text{Au}(100)$  surface after 800 L of  $\text{O}_2$  exposure at 350  
2 °C. (b) STM line profile along the white dashed line across the CuAu terrace (Y) and the adjacent  
3 oxygenated Cu terraces (X, Z) in (a). (c) Atomically zoomed-in STM image (size:  $2 \times 2 \text{ nm}^2$ ) of the  
4 oxygenated Cu terrace marked with white dashed box c in (a), inset is the  $c(2 \times 2)\text{-O}$  structure overlaid on  
5 the STM image. (d) Zoomed-in STM image (size:  $40 \times 40 \text{ nm}^2$ ) of the stepped region marked with white  
6 dashed box d in (a), overlaid onto the STM image is the adsorption of O atoms onto the four-fold hollow  
7 sites made by the Cu atoms at the step edge. The blue and red balls represent Cu and O atoms,  
8 respectively. (e) STM line profile along the white dashed line along the step edge of the  $c(2 \times 2)\text{-O}$  terrace  
9 in (d). The tunneling conditions for STM imaging: (a)  $V_B = 2 \text{ V}$ ,  $I_T = 0.1 \text{ nA}$ , (c, d)  $V_B = 0.35 \text{ V}$ ,  $I_T = 1 \text{ nA}$ .  
10

11 Fig. 4 corresponds to the longer  $\text{O}_2$  exposure (1800 L) that results in the significant area  
12 shrinkage of CuAu-terminated terraces. As marked in Fig. 4(a), the extension of the lateral size  
13 of the oxygenated Cu terraces increases up to  $\sim 80 \text{ nm}$  while the CuAu terraces shrink in size to  
14 as small as  $\sim 5 \text{ nm}$  in some regions. Meanwhile, Fig. 4(a) also shows that the oxygenated Cu  
15 terraces have a high density of clusters whereas the CuAu terraces are relatively free of clusters.  
16 As marked by the arrows, long and thin strips are also formed in the oxygenated Cu terraces. Fig.  
17 4(b) displays the STM height profile along the white dashed line across an oxygenated Cu terrace  
18 and its upper and lower CuAu terraces in Fig. 4(a), where the step heights of  $\sim 1.71 \text{ \AA}$  and  $\sim 2.01$   
19  $\text{ \AA}$  are consistent with the monatomic step heights between the upper CuAu terrace (A) and the  
20 wide lower oxygenated Cu terrace and the monatomic step between the oxygenated Cu terrace  
21 (B) and the bottom CuAu terrace (C), respectively. Fig. 4(c) shows an atomically zoomed-in STM  
22 image of the region marked with white dashed box c in Fig. 4(a), which confirms the  $c(2 \times 2)\text{-O}$   
23 superstructure formed in the oxygenated Cu terrace. Clusters with a lateral size of  $\sim 4 \text{ \AA}$  are also  
24 visible in the STM image and the surface height of clusters are revealed later by the STM line  
25 profile (Fig. 4(e)).

26 Fig. 4(d) shows a zoomed-in STM image of the region with a long strip in the  $c(2 \times 2)\text{-O}$   
27 oxygenated Cu terrace, as marked with white dashed box d in Fig. 4(a). The atomic structure of  
28 these long bright strips cannot be resolved clearly from the STM image. Fig. 4(e) illustrates the

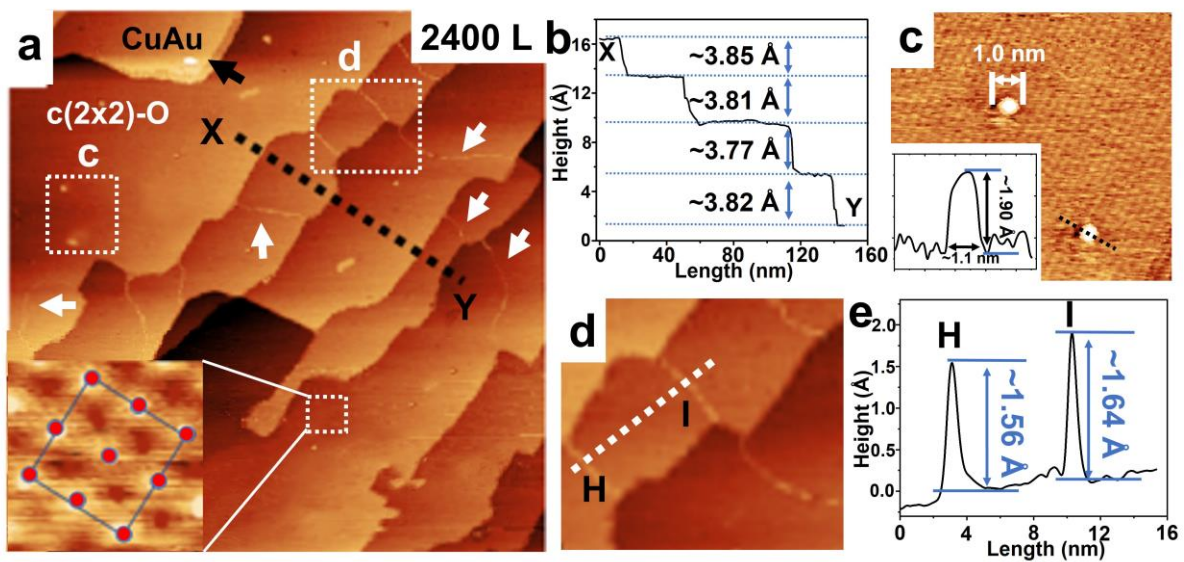
1 STM height profile across the strip and clusters as marked by the thin rectangle in Fig. 4(d),  
 2 showing a similar surface height of  $\sim 1.34 \pm 0.02$  Å for the cluster (H) and strip (I). The similar  
 3 surface heights of the strips and clusters suggest that they are composed of the same type of  
 4 atomic species. As elucidated later by XPS analysis in Fig. 6 and DFT modeling in Fig. 9, these  
 5 strips and clusters are composed of Cu atoms and formed via the aggregation of Cu adatoms  
 6 generated from O-attack induced decomposition of the CuAu terraces (the decomposition of the  
 7 CuAu terraces also results in Au adatoms that dissolve in the bulk because of the lack of oxygen  
 8 affinity for Au). The absence of the clusters on the CuAu terraces indicates that Cu adatoms prefer  
 9 to stay on the  $c(2 \times 2)$ -O terraces rather than on the CuAu terraces due to the anchoring effect  
 10 from the adsorbed O on stabilizing the clusters of Cu adatoms.



11  
 12 **Fig. 4:** (a) STM image (size:  $300 \times 300$  nm<sup>2</sup>) of the Cu<sub>3</sub>Au(100) surface after 1800 L of O<sub>2</sub> exposure at  
 13 350 °C. (b) STM line profile along the white dashed line across the oxygenated Cu terrace (B) and its upper  
 14 and lower oxygenated Cu terraces (A, C) in (a). (c) Atomically zoomed-in STM image (size:  $3 \times 3$  nm<sup>2</sup>) of  
 15 the oxygenated Cu terrace marked with white dashed box c in (a), showing the formation of Cu clusters on  
 16 the Cu-terminated  $c(2 \times 2)$ -O surface. (d) Zoomed-in STM image (size:  $40 \times 40$  nm<sup>2</sup>) of the region consisting  
 17 of a Cu strip and Cu clusters, as marked with white dashed box d in (a). (e) STM line profile across the Cu  
 18 strip and Cu clusters as marked by the thin rectangle in (d), showing their similar surface heights of  $\sim 1.3$   
 19 Å. The tunneling conditions for STM imaging: (a, d)  $V_B = 2$  V,  $I_T = 0.1$  nA, (c)  $V_B = 0.1$  V,  $I_T = 1$  nA.

20

1 Fig. 5(a) displays an STM image of the surface morphology after 2400 L of the O<sub>2</sub>  
 2 exposure. Compared to the lower O<sub>2</sub> exposures shown above, the surface now has improved  
 3 smoothness with the more straightened morphology of the step edges. Meanwhile, the number  
 4 density of Cu clusters is significantly reduced, but with an increased average size. As indicated  
 5 by white arrows, each terrace has long bright strips of Cu adatoms, suggesting nearly complete  
 6 decomposition of all the CuAu terraces, thereby transforming almost the entire surface to the  
 7 oxygenated Cu termination. This is confirmed by the atomically zoomed-in STM image (the  
 8 bottom-left inset of Fig. 5(a)), showing the formation of the  $c(2\times 2)$ -O superstructure by O  
 9 adsorption into the hollow sites of the Cu terraces. The upper-left corner region (marked with the  
 10 black arrow) shows a very small terrace, which is a reminder of the undecomposed CuAu terrace.  
 11 The decomposition of the CuAu terraces also transforms the monatomic steps between adjacent  
 12 CuAu and Cu terraces into bilayer atomic steps. This is confirmed by measuring the step heights  
 13 across the different terraces in Fig. 5(b), where the surface profile is obtained along the black  
 14 dashed line in Fig. 5(a). All the steps now have the surface height of  $\sim 3.81\pm 0.04$  Å, which is the  
 15 sum of the heights of monatomic steps shown in Figs. 2-4.



16

1 **Fig. 5:** (a) STM image (size:  $300 \times 300 \text{ nm}^2$ ) of the  $\text{Cu}_3\text{Au}(100)$  surface after 2400 L of  $\text{O}_2$  exposure at  
2 350 °C. The white arrows mark the formation of Cu strips in the oxygenated Cu terraces. The black arrow  
3 marks the remaining, undecomposed CuAu terrace. The bottom-left inset is an atomically zoomed-in STM  
4 image (size:  $1.5 \times 1.5 \text{ nm}^2$ ) of the oxygenated Cu terrace, overlaid onto the STM image is the  $c(2 \times 2)$ -O  
5 superstructure. (b) STM line profile along the black dashed line across the multiple terraces in (a). (c)  
6 Zoomed-in STM image (size:  $10 \times 10 \text{ nm}^2$ ) of the region with Cu clusters, as marked with white dashed box  
7 c in (a). The bottom-left inset is the surface height profile along the black dashed line across a Cu cluster.  
8 (d) Zoomed-in STM image (size:  $20 \times 20 \text{ nm}^2$ ) of the region with Cu strips, as marked with white dashed  
9 box d in (a). (e) STM surface profile along the white dashed line across Cu strips H and I in (d), showing  
10 their similar surface heights of  $\sim 1.5 \text{ \AA}$  and  $\sim 1.6 \text{ \AA}$ , respectively. The tunneling conditions for STM imaging:  
11 (a, d)  $V_B = 1.5 \text{ V}$ ,  $I_T = 0.1 \text{ nA}$ , (c)  $V_B = 0.1 \text{ V}$ ,  $I_T = 1 \text{ nA}$ .

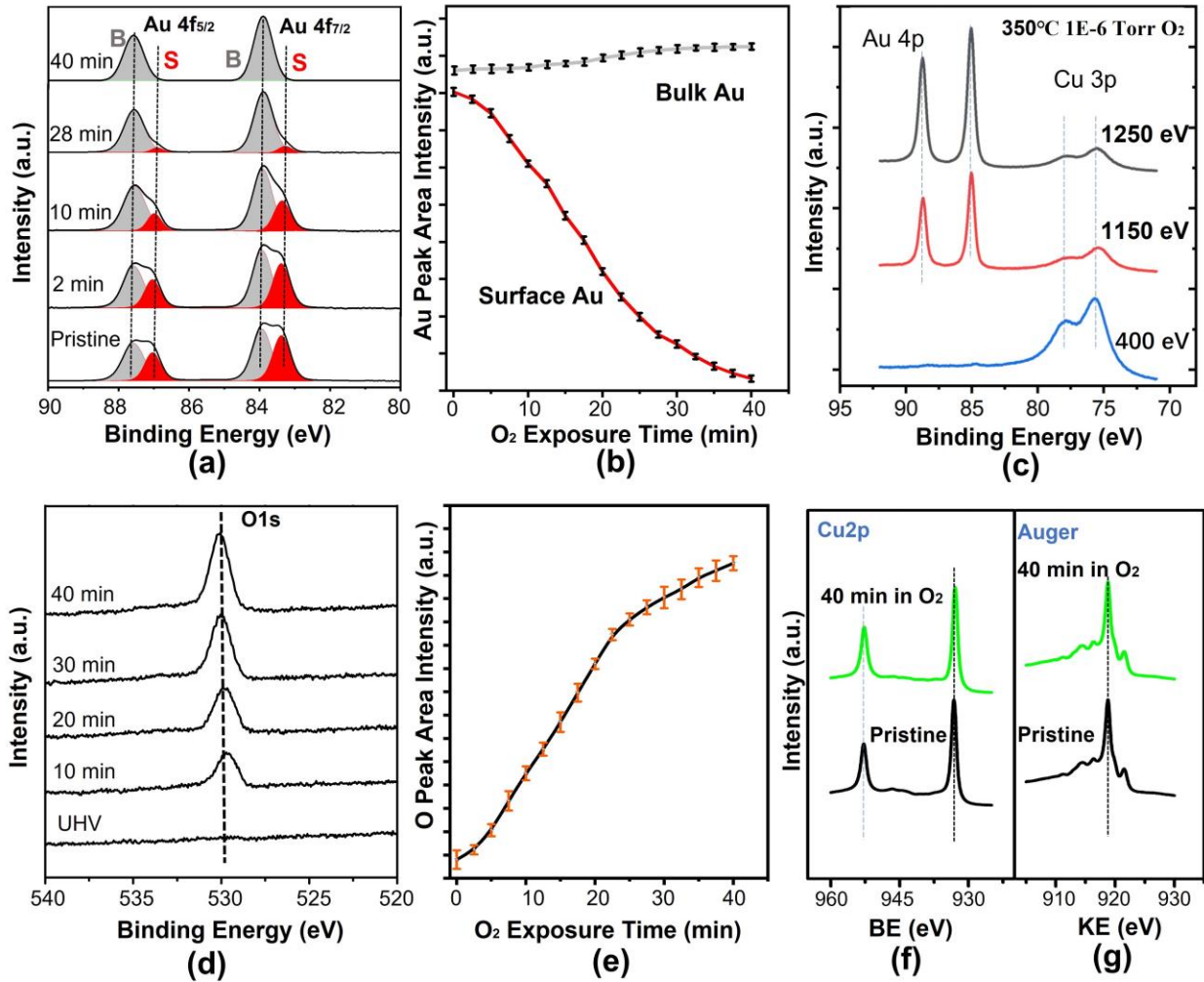
12  
13 Fig. 5(c) is an atomically resolved STM image of the oxygenated Cu terrace as marked  
14 with white dashed box c in Fig. 5(a), confirming the presence of Cu clusters on the  $c(2 \times 2)$ -O  
15 surface. The upper-right inset of Fig. 5(a) is a line profile across the Cu cluster marked by the  
16 black dashed line, showing a surface height of  $\sim 1.90 \text{ \AA}$  and a lateral size of  $\sim 1.1 \text{ nm}$ . Fig. 5(d)  
17 shows a zoomed-in STM image of the region containing several strips in the  $c(2 \times 2)$ -O terrace, as  
18 marked with white dashed box d in Fig. 5(a). Fig. 5(e) is the STM line profile along the white  
19 dashed line across two strips (H, I) marked in Fig. 5(d), showing the strip heights of  $\sim 1.60 \pm 0.04$   
20  $\text{ \AA}$ , which are  $\sim 0.3 \text{ \AA}$  higher than the surface height ( $\sim 1.34 \text{ \AA}$ ) of the strips for the shorter time of  
21 the  $\text{O}_2$  annealing (Fig. 4(e)). As opposed to the lower  $\text{O}_2$  exposures, the increased sizes (both  
22 laterally and vertically) of the clusters and strips are induced by a three-dimensional ripening  
23 process of Cu adatoms during the prolonged  $\text{O}_2$  annealing, which results in fewer but larger  
24 clusters as shown in Fig. 5(a). STM imaging of the  $\text{Cu}_3\text{Au}(100)$  surface after the  $\text{O}_2$  exposure at  
25 100 °C shows the similar behavior of the oxygen adsorption induced decomposition of the topmost  
26 CuAu plane (data not shown), albeit with a slower kinetics.

27

## 28 **3.2 AP-XPS measurements**

1 To complement the above STM observations that provide microscopic information on the  
2 surface morphology and atomic structure changes induced by the oxygen attack, AP-XPS is  
3 employed to monitor the temporal evolution of surface composition and chemical state during the  
4 O<sub>2</sub> exposure. As shown in Fig. 6(a), the Au 4f region of the XPS spectra obtained from the pristine  
5 Cu<sub>3</sub>Au(100) (under UHV) consists of Au 4f<sub>7/2</sub> and Au 4f<sub>5/2</sub>, each of which can be deconvoluted into  
6 two components, located at the binding energies of 84.0 eV and 83.5 eV for Au 4f<sub>7/2</sub> and 87.5 eV  
7 and 87.0 eV for Au 4f<sub>5/2</sub>, respectively. As marked in Fig. 6(a), the two components correspond to  
8 surface (S) Au and bulk (B) Au, and their binding energies are consistent with previous work on  
9 the Cu-Au alloys [12,20,32,33]. Fig. 6(a) illustrates that the peak intensity of the surface Au  
10 component decreases gradually upon the continued exposure of the Cu<sub>3</sub>Au(100) to pO<sub>2</sub>=1×10<sup>-6</sup>  
11 Torr and 350 °C. After ~ 40 min of the O<sub>2</sub> exposure, the surface Au peak disappears completely.  
12 By contrast, the bulk Au component only has a slight increase in the peak intensity and its binding  
13 energy remains the same at 84 eV. This is further evident from the temporal evolution of the  
14 integrated intensities of the surface Au and bulk Au peaks in Fig. 6(b), which shows that the peak  
15 intensity for surface Au drops quickly while the peak intensity of bulk Au only increases slightly  
16 and then reaches a saturated level during the continued O<sub>2</sub> exposure. As illustrated from the STM  
17 imaging in Figs. 2-5, the O adsorption leads to the decomposition of CuAu terraces, which results  
18 in Cu and Au adatoms. As shown here by the XPS measurements, the complete disappearance  
19 of the surface Au peak reveals that Au adatoms actually dissolve into the bulk and the surface  
20 clusters observed in the STM images (Figs. 3-5) are formed by the aggregation of Cu adatoms  
21 supplied from the decomposing CuAu terraces. Meanwhile, the relatively constant intensity of the  
22 bulk Au peak indicates that Au travels into the deeper subsurface region. Meanwhile, the O<sub>2</sub>  
23 induced surface termination of Cu is further confirmed by XPS measurements with different  
24 incident photon energies. As shown in Fig. 6(c), the Au 4f and Cu 3p region taken with the lower

1 photon energy of 400 eV shows the absence of Au 4f signal, suggesting that the top surface is  
 2 terminated as nearly pure Cu. The Au 4f peak emerges stronger in intensity with the higher photon  
 3 energies of 1150 eV and 1250 eV, indicating the higher Au concentration in the deeper subsurface  
 4 region.



5  
 6 **Fig. 6:** (a) Temporal evolution of Au-4f XPS spectra taken with the incident photon energy of 400 eV during  
 7 the exposure of the Cu<sub>3</sub>Au(100) at 350 °C to pO<sub>2</sub>=1×10<sup>-6</sup> Torr. S (in red) and B (in grey) correspond to the  
 8 surface Au and bulk Au contributions, respectively. (b) Evolution of the integrated area of the surface Au  
 9 and bulk Au peaks as a function of O<sub>2</sub> exposure time. (c) Au 4f and Cu 3p spectra of the Cu<sub>3</sub>Au(100)  
 10 measured at 350 °C and pO<sub>2</sub>=1×10<sup>-6</sup> Torr with the incident photon energies of 400, 1150, and 1250 eV,

1 respectively. **(d)** Temporal evolution of O 1s spectra taken with the incident photon energy of 650 eV during  
2 the exposure of the Cu<sub>3</sub>Au(100) at 350 °C to pO<sub>2</sub>=1×10<sup>-6</sup> Torr. **(e)** Integrated intensities of the O 1s spectra  
3 during the continued O<sub>2</sub> exposure. **(f, g)** Cu 2p and Cu L<sub>3</sub>M<sub>45</sub>M<sub>45</sub> spectra confirming the metallic state of Cu  
4 during the O<sub>2</sub> dosing.

5  
6 The oxygen-attack induced decomposition of CuAu-terminated terraces is corroborated  
7 by monitoring the corresponding O 1s spectra as a function of the O<sub>2</sub> exposure (Fig. 6(d)). The  
8 pristine surface is O-free, as confirmed by the absence of any detectable intensity from the O 1s  
9 region under UHV (the bottom panel in Fig. 6(d)). Exposure to pO<sub>2</sub>=1×10<sup>-6</sup> Torr and 350 °C (same  
10 as the STM experiments above) results in appreciable intensity in the O 1s core level, indicating  
11 the O uptake by chemisorption that results in the c(2×2)-O superstructure on Cu-terminated  
12 terraces, as shown by the above STM imaging (Figs. 2-5)). Fig. 6(e) corresponds to the evolution  
13 of the integrated intensities of the O 1s spectra as a function of the O<sub>2</sub> exposure time. By  
14 combining the STM imaging shown in Figs. 2-5, it can be known that the continued increase in  
15 the O 1s intensity is caused by the c(2×2)-O formation on Cu-terminated terraces and the O-  
16 attack induced decomposition of CuAu terraces, where the latter results in the formation of  
17 monatomic depressions with the c(2×2)-O formation on the exposed Cu plane of the bottom of  
18 the surface pits. Figs. 6(d, e) show that continued O<sub>2</sub> exposure brings stronger intensity to the O  
19 1s spectra but does not induce noticeable changes in the peak position, confirming that the  
20 oxidation condition (pO<sub>2</sub>, T) employed here allows for building up more chemisorbed O on the  
21 surface but is not sufficient to drive the transformation of the c(2×2)-O to other O chemisorbed  
22 phases (such as the  $(2\sqrt{2} \times \sqrt{2})R45^\circ - 0$  missing-row reconstruction) or bulk oxide formation, as  
23 observed from the oxidation pathway of Cu(100) [13,29,34–36]. The surface oxidation not going  
24 beyond c(2×2)-O is also confirmed by the coordinated Cu 2p (Fig. 6(f)), where the shape and

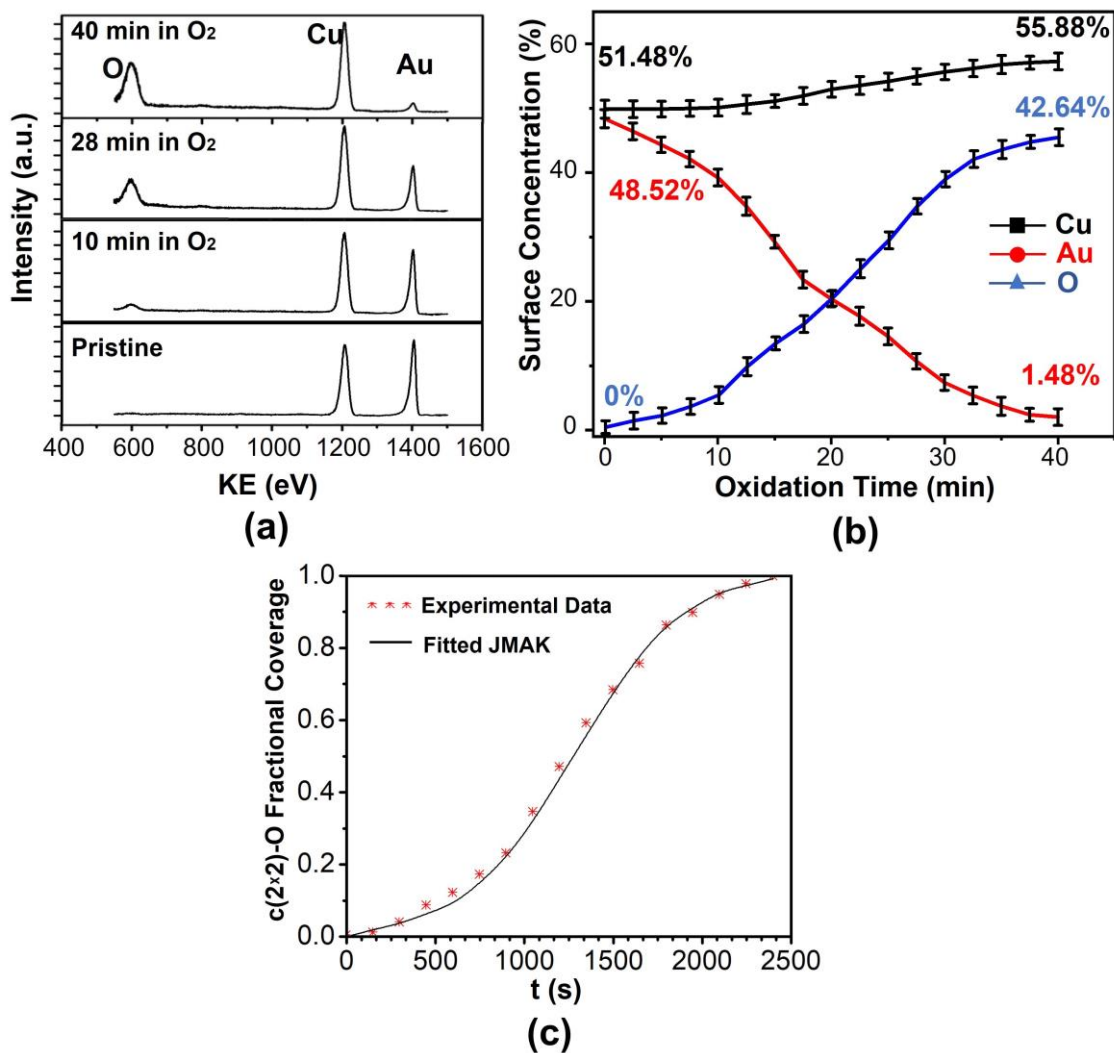
1 position of the Cu 2p core level peaks remain the same for the pristine and the O<sub>2</sub>-exposed  
2 surfaces, indicating that Cu remains its metallic state. This is further corroborated by the Cu  
3 L3M<sub>45</sub>M<sub>45</sub> Auger spectra that are also acquired to confirm the valence states of Cu, as shown in  
4 Fig. 6(g). The pristine Cu<sub>3</sub>Au(100) surface shows the Cu LMM line peak at a kinetic energy (KE)  
5 of 918.6 eV, which is associated with metallic Cu<sup>0</sup>. The subsequent O<sub>2</sub> exposure at pO<sub>2</sub>=1×10<sup>-6</sup>  
6 Torr and 350 °C results in no changes in the line position and shape of the Cu LMM spectra. The  
7 combined STM, XPS, and Auger measurements confirm that Cu largely maintains its metallic  
8 state (Cu<sup>0</sup>) although the surface is covered with chemisorbed O.

9

### 10 **3.3 LEIS measurements**

11 To complement the XPS measurements of the surface composition averaged over a few  
12 atomic layers (i.e., the thickness corresponding to the mean free path of photoelectrons), LEIS is  
13 also performed to monitor the O adsorption induced composition evolution in the topmost atomic  
14 layer only. The LEIS spectra are taken with 1499 eV He<sup>+</sup> and the scattering angle of 135°, under  
15 which a good mass separation between Au and Cu can be ensured in combination with a high  
16 detector efficiency. We firstly measure the ISS spectra from pure Cu and pure Au samples to  
17 obtain the elemental sensitivity factors. The elemental sensitivity factor does not depend on the  
18 chemical environment of an atom in the surface [37]. The surface composition of the Cu<sub>3</sub>Au(100)  
19 can be directly quantified with the ISS peak intensities modified by the sensitivity factor of Cu and  
20 Au. Fig. 7(a) shows the LEIS spectra, in which the three peaks located at KE = 626 eV, 1209 eV  
21 and 1399 eV correspond to O, Cu and Au, respectively. For the pristine surface under UHV, there  
22 is no detectable O signal, and the Cu and Au peaks show similar intensity. Upon switching from  
23 the UHV to O<sub>2</sub> gas at pO<sub>2</sub>=1×10<sup>-6</sup> Torr and 350 °C, the O peak becomes visible, and its intensity

1 increases with the continued O<sub>2</sub> exposure. By contrast, the intensity of the Au peak decreases  
 2 and becomes nearly invisible after ~ 40 min of the O<sub>2</sub> exposure.



3  
 4 **Figure 7.** (a) Temporal evolution of LEIS spectra obtained from the Cu<sub>3</sub>Au(100) during the exposure of the  
 5 Cu<sub>3</sub>Au(100) at 350 °C to pO<sub>2</sub>=1×10<sup>-6</sup> Torr. (b) Evolution of the composition of Au, Cu, and O in the topmost  
 6 surface layer as a function of the O<sub>2</sub> exposure time. (c) Evolution of the c(2×2)-O fractional area coverage  
 7 as a function of the O<sub>2</sub> exposure time, and its fit to the JMAK equation,  $X(t) = 1 - \exp(-kt^n)$ ,  
 8 where  $n = 2$  and  $k = 3.8 \times 10^{-7} \text{ s}^{-2}$ .  
 9

10 Fig. 7(b) illustrates the surface composition evolution by quantifying the integrated peak  
 11 areas of O, Cu and Au in the LEIS spectra modified by corresponding atomic sensitive factor in

1 Fig. 7(a), showing that the O concentration increases whereas the Au concentration decreases  
2 as a function of the O<sub>2</sub> exposure. This indicates an increased O amount in the topmost whereas  
3 a decreased net amount of Au amount in the topmost surface with the continued O<sub>2</sub> exposure,  
4 consistent with the trend derived from the XPS measurements in Fig. 6. It can be also noted from  
5 Fig. 7(b) that the Cu composition is slightly higher than the Au composition for the pristine surface,  
6 which is consistent with the STM observation showing that the pristine surface is dominated by  
7 CuAu terraces (consisting of equal numbers of Cu and Au atoms) along with narrow terraces  
8 having the surface termination of the pure Cu plane (Fig. 1). Fig. 7(b) also shows that the Cu  
9 concentration increases from ~52% in the beginning to ~ 56% at the end of the O<sub>2</sub> exposure (~  
10 40 min), corroborating well with the STM observations (Figs. 3-5) of Cu clusters and strips formed  
11 by the aggregation of Cu adatoms supplied from decomposing CuAu terraces. Meanwhile, the  
12 decreased Au concentration and its disappearance at the end also confirm the dissolution of Au  
13 adatoms from the decomposing CuAu terraces into the bulk of the Cu<sub>3</sub>Au crystal.

14

### 15 **3.4 JMAK fit of the oxygen chemisorption kinetics**

16 The O chemisorption on the Cu<sub>3</sub>Au(100) occurs via a nucleation and growth process. This  
17 is evidenced by the formation and growth of monatomic depressions of  $c(2\times 2)$ -O domains in CuAu  
18 terraces from our STM observations (Figs. 2-5). This is also consistent with previous studies  
19 suggesting the nucleation and growth mechanism for oxygen-chemisorption induced surface  
20 phase transformations on the Cu(110) surface [38,39]. Kinetics of the phase transformations that  
21 occur via nucleation and growth is commonly addressed through the classic theory of Johnson-  
22 Mehl-Avrami-Kolmogorov (JMAK) [40,41]. For phase transformations in two-dimensional systems  
23 (like surfaces), the JMAK theory assumes that the fractional coverage of the transformed area,  
24  $X(t)$ , follows an exponential dependence on time  $t$

$$X(t) = 1 - \exp(-kt^n), \quad (2)$$

where  $n$  is the Avrami exponent, and  $k$  is the reaction rate constant. The Avrami exponent contains information about nucleation mechanisms and growth dimensionality ( $D$ ). Nucleation mechanisms can be categorized based on how frequent nucleation occurs in the system. If the formation of nuclei happens only at the beginning of the transformation period and growth takes place afterwards, it would then be identified as a site-saturate nucleation, and  $n = D$ . By contrast, if the system keeps adding nuclei with a constant rate over the entire transformation period, it would be characterized as the constant nucleation rate mechanism, and  $n = D + 1$ . The rate constant, on the other hand, is computed as  $k = \pi v^2 N$  for site saturated nucleation and  $k \sim \pi v^2 \dot{N}$ , where  $N$  is nucleation density,  $\dot{N}$  constant nucleation rate and  $v$  the constant interface velocity.

The evolution of the  $c(2 \times 2)$ -O fractional area coverage can be obtained using the LEIS-measured surface composition of O shown in Fig. 7(b) and by calibrating against the O concentration at the saturated  $c(2 \times 2)$ -O coverage (=1). Fig. 7(c) shows the plot of the  $c(2 \times 2)$ -O fractional area coverage with respect to the  $O_2$  exposure time. The solid line is the best fit to the JMAK equation (Eq. 2), where  $n = 2$ ,  $k = 3.8 \times 10^{-7} \text{ s}^{-2}$ . Based on the  $c(2 \times 2)$ -O fractional area coverage evolution (Fig. 7(c)), we can present a physical picture of nucleation and growth for linking the STM imaging (Figs. 2-5) to the JMAK fitting parameters. The Avrami exponent value,  $n = 2$ , obtained from the JMAK fitting indicates a site-saturate nucleation mechanism of  $c(2 \times 2)$ -O, which corroborates well with the STM results. As shown in Fig. 1, the pristine  $Cu_3Au(100)$  surface consists of wide CuAu terraces and narrow Cu terraces. After 200 L of  $O_2$  exposure, the surface is oxidized into the  $c(2 \times 2)$ -O for the Cu terraces and depressions within the CuAu terraces. Therefore, the nucleation density of  $c(2 \times 2)$ -O can be determined by counting the number density of Cu terraces and depressions in the STM images. As shown in Figs. 2-5, the surface densities of  $c(2 \times 2)$ -O nuclei can be determined as  $N = 3.6 \times 10^{-4} \text{ nm}^{-2}$ ,  $4.0 \times 10^{-4} \text{ nm}^{-2}$ , and  $3.9 \times 10^{-4} \text{ nm}^{-2}$ ,

1 for the O<sub>2</sub> exposures of 200 L, 800 L, and 1800 L, respectively. This indicates that the c(2×2)-O  
2 nucleation happens only at the beginning of the O<sub>2</sub> exposure, and the continued O<sub>2</sub> exposure only  
3 leads to the growth of nucleated c(2×2)-O domains. This site-saturated nucleation behavior  
4 suggests a surface diffusion mechanism of oxygen that results in an active zone of capture of  
5 oxygen around each c(2×2)-O nucleus. That is, oxygen landing inside this capture zone may  
6 migrate to the c(2×2)-O nucleus, leading to the growth of the c(2×2)-O nucleus rather than  
7 nucleating a new c(2×2)-O cluster. Therefore, there is a saturated number density of c(2×2)-O  
8 clusters due to the competition for the capture of diffusing O on the surface. Meanwhile, we can  
9 also obtain experimentally the value of the fit parameter of the rate constant,  $k = (\pi)v^2N$ , from  
10 the analysis of the STM imaging of nucleation and growth of c(2×2)-O clusters. As measured from  
11 the STM images in Figs. 2-5, the values for the saturated nucleation density and the constant  
12 interface velocity can be determined as  $N = \sim 3.83 \times 10^{-4} \text{ nm}^{-2}$  and  $v = \sim 8.6 \times 10^{-2} \text{ nm} \cdot \text{s}^{-1}$  (by  
13 approximating a circular shape of the c(2×2)-O clusters). Therefore, the rate constant k has the  
14 value of  $k = 3.31 \times 10^{-7} \text{ s}^{-2}$ , which matches very well with that ( $k = 3.8 \times 10^{-7} \text{ s}^{-2}$ ) from the JMAK  
15 fitting in Fig. 7(c). This excellent agreement between the experiments (STM and LEIS) and the  
16 JMAK fitting demonstrates that the surface diffusion of oxygen is the dominant mechanism  
17 underlying the experimentally observed site saturated nucleation and 2D growth kinetics of  
18 c(2×2)-O domains.

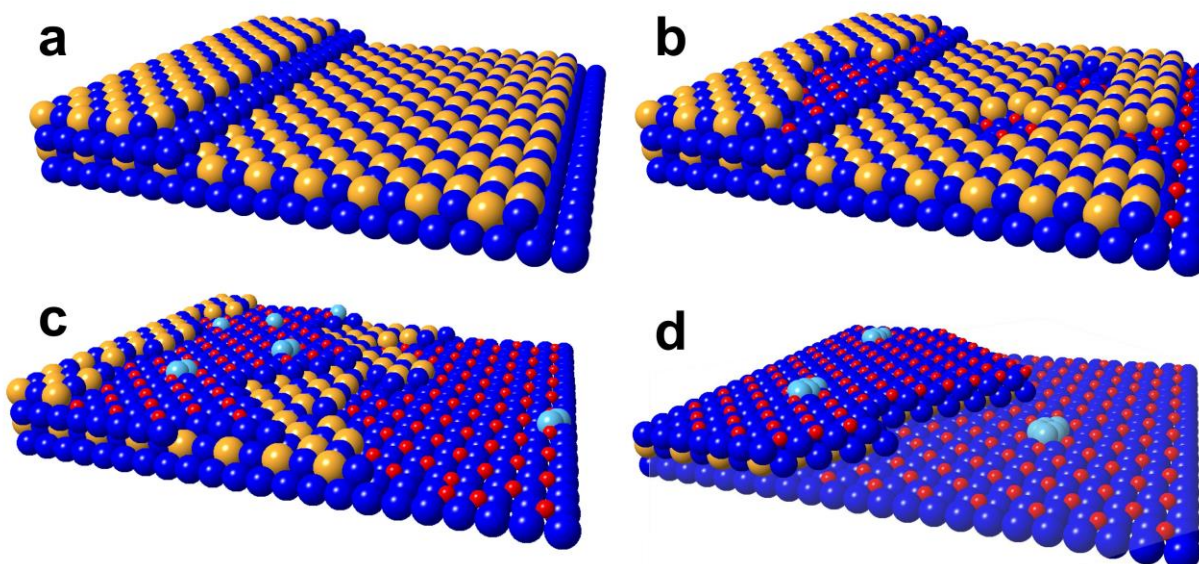
19

### 20 **3.5 DFT modeling**

21 The experiments and analysis shown above demonstrate that the initial oxidation of  
22 Cu<sub>3</sub>Au(100) begins with the nucleation and growth of c(2×2)-O domains. Fig. 8 schematizes the  
23 key feature of the microscopic processes as identified from STM observations. The pristine

1 surface consists of narrow Cu terraces and wide CuAu terraces, which are separated by single-  
2 atomic-height steps (Fig. 8a). The O adsorption results in the nucleation of  $c(2\times 2)$ -O domains on  
3 the Cu terraces and within the CuAu terraces by locally decomposing the topmost CuAu layer,  
4 thereby exposing the underlying Cu plane and forming monatomic depressions (Fig. 8(b)). The  
5 continued  $O_2$  exposure leads to the growth of  $c(2\times 2)$ -O domains via the receding motion of the  
6 monatomic steps of CuAu terraces (Fig. 8(c)). The O adsorption induced decomposition of the  
7 CuAu terraces transforms the entire surface into Cu(100)-like,  $c(2\times 2)$ -O terminated terraces  
8 separated by double-atomic-height steps (Fig. 8(d)). Although the above microscopic processes  
9 are revealed from the STM observations, two questions naturally arise as to (i) why monatomic  
10 CuAu steps undergo receding motion to expose the underlying Cu plane and (ii) how monatomic  
11 depressions form within CuAu terraces, both of which requires decomposing CuAu terraces. We  
12 attribute the CuAu decomposition to O adsorption along the step edge and within the CuAu  
13 terraces, which results in the abstraction of Cu and Au atoms surrounding the adsorbed O.

14



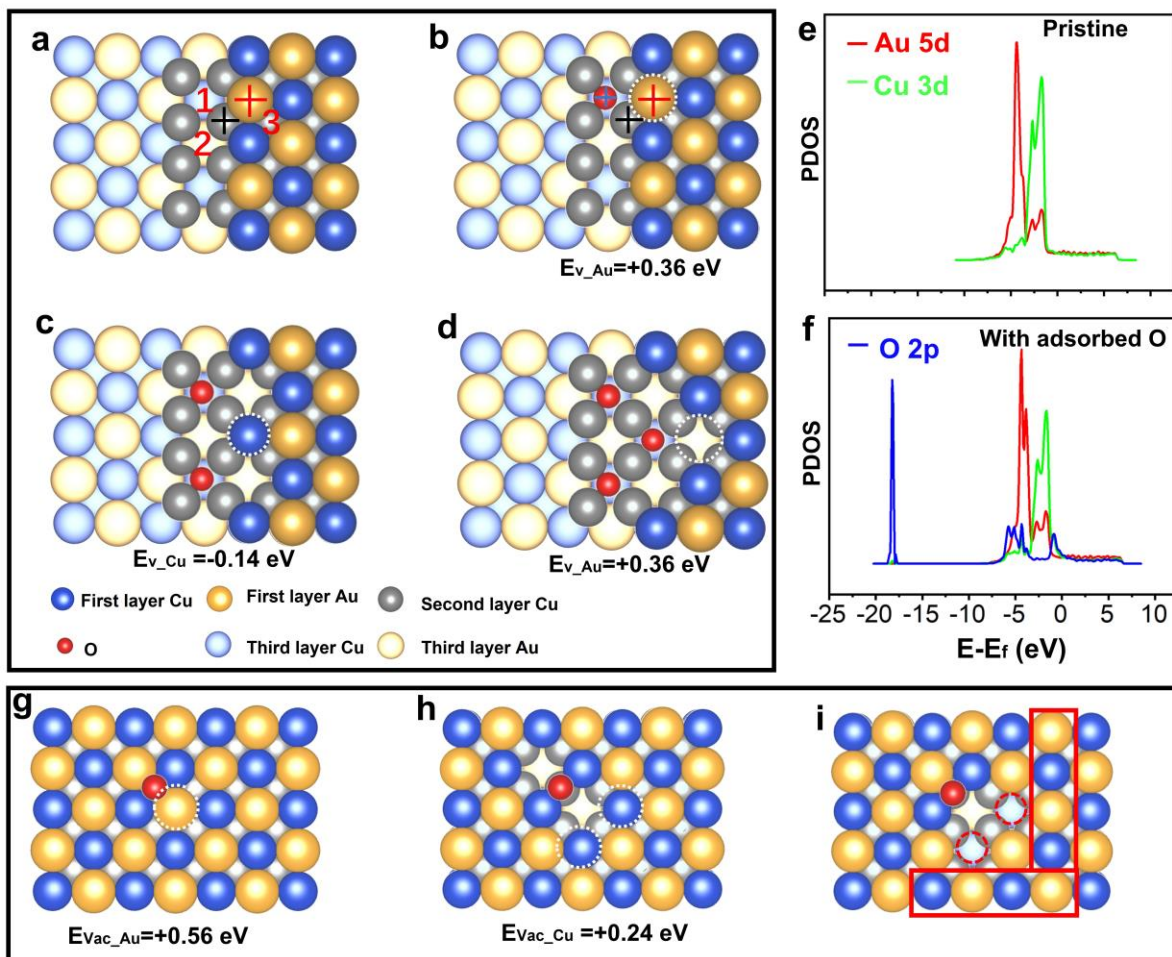
15

1 **Fig. 8.** Schematic illustrations showing the microscopic processes of the initial-stage oxidation of  
2  $\text{Cu}_3\text{Au}(100)$ . (a) Pristine  $\text{Cu}_3\text{Au}(100)$  consisting of wide CuAu terraces and narrow Cu terraces separated  
3 by monoatomic steps. (b)  $\text{O}_2$  exposure results in the nucleation of  $c(2\times 2)$ -O domains by O adsorption into  
4 four-fold hollow sites of Cu terraces and O-adsorption induced formation of surface pits in CuAu terraces.  
5 (c) The growth of  $c(2\times 2)$ -O domains occurs via O-adsorption induced decomposition of CuAu terraces via  
6 the receding motion of atomic steps, which results in Cu adatoms (aggregating into Cu clusters) and Au  
7 adatoms (dissolving into the bulk). (d) O adsorption induced complete decomposition of CuAu terraces  
8 transforms the entire surface into Cu(100)-like,  $c(2\times 2)$ -O terminated terraces separated by double-atomic-  
9 height steps along with the formation of Cu clusters on the surface. Yellow, blue, and red balls represent  
10 Au, Cu, and O atoms, respectively, and light blue balls stand for Cu adatoms.  
11

12 To further substantiate the O adsorption effect on the CuAu decomposition, we employ  
13 DFT computation to evaluate the relative stability of Cu and Au atoms in the vicinity of adsorbed  
14 O along the step edge and on the CuAu terrace. As known from the STM images in Figs. 1-6, the  
15 preferred terrace edge orientation is along the  $[110]$  direction. Fig. 9(a) shows the atomic structure  
16 of the  $[110]$  step consisting of the lower Cu(100) terrace and the upper CuAu(100) terrace. There  
17 are three crystallographically nonequivalent four-fold hollow sites for O adsorption along the step  
18 edge, as marked “1”, “2”, and “3” in Fig. 9(a). The O adsorption energies for these three sites are  
19 calculated to be -1.89 eV, -1.71 eV, -0.92 eV, respectively. Therefore, site “1”, which has five  
20 coordinating Cu atoms (four in the Cu terrace and one beneath), is energetically most favorable  
21 for O adsorption because of the larger O affinity of Cu than Au. The presence of the adsorbed O  
22 at site “1” also promotes the step-edge detachment of the adjacent Au on the upper terrace, as  
23 marked by the white dashed circle in Fig. 9(b). This is confirmed by DFT computations showing  
24 the significant decrease in the vacancy formation energy of the step-edge Au atom from 0.74 eV  
25 (before the O adsorption) to 0.36 eV (after the O adsorption), which is lower enough for the Au  
26 atom to detach from the step edge at the elevated temperature of the experiment (350 °C). In the  
27 same way, another O atom is adsorbed into the nearest equivalent four-fold hollow site that also  
28 has five coordinating Cu atoms, thereby inducing the step-edge detachment of the Au atom on  
29 the upper terrace, as shown in Fig. 9(c)). Upon the departure of the two Au atoms, the step-edge

1 Cu atom, as marked by the white dashed circle in Fig. 9(c), becomes significantly  
2 undercoordinated and detaches spontaneously from the step edge (with the vacancy formation  
3 energy of -0.14 eV). The O-adsorption induced step-edge detachment of the Au and Cu atoms  
4 exposes the underlying Cu plane, and this leads to the extension of the lower Cu terrace by the  
5 same way of adsorbing O atoms to the similar four-fold hollow sites with five coordinating Cu  
6 atoms (Fig. 9(d)).

7 The O adsorption induced step-edge detachment is further elucidated by the projected  
8 density of states (PDOS) of the 3d, 5d orbitals of the Cu and Au atoms and O 2p of chemisorbed  
9 O. As shown in Fig. 9(e), the Cu 3d band overlaps with the Au 5d band below the Fermi level,  
10 indicating the Cu 3d-Au 5d hybridization for the pristine step (Fig. 9(a)). Fig. 9(f) corresponds to  
11 the PDOS plots obtained from the step with adsorbed O adjacent to the Au atom (Fig. 9(b)),  
12 showing the hybridization between Cu 3d and O 2p at -19 eV and near the Fermi level region.  
13 Compared to the pristine step, the density states of Cu 3d decrease in the Cu 3d-Au 5d  
14 hybridization region, and the broadening of the Cu 3d band results in a tiny density shoulder near  
15 the Fermi level to overlap with O 2p, indicating the weakening of the Cu-Au bond because of the  
16 decreased charge transfer from Cu to Au. This is also confirmed by the Bader charge analysis of  
17 the pristine and O adsorbed steps. The Cu and Au atoms within the pristine step have the Bader  
18 charges of 10.89e and 11.35e, respectively. The O adsorption at the step edge (Fig. 9(b)) results  
19 in a large decrease in the Bader charge of the Cu atom to 10.66e but a smaller increase (11.31  
20 eV) by the Au atom. This indicates the increased electron transfer from Cu to O but decreased  
21 electron gain by Au.



1  
2 **Fig. 9.** DFT modeling of O-adsorption-induced AuCu decomposition via step-edge and in-terrace  
3 detachment. (a) Stepped Cu<sub>3</sub>Au(100) surface consisting of Cu-terminated and CuAu-terminated terraces  
4 separated by monatomic steps with the terrace edge orientation along the [110] direction. Three  
5 crystallographically nonequivalent four-fold hollow sites are identified for O adsorption in the vicinity of the  
6 step edge. (b) O preferentially adsorbs at hollow site “1” consisting of five coordinating Cu atoms,  
7 destabilizing the adjacent Au atom (marked by the white dashed circle) on the upper terrace. (c) The  
8 departure of the second Au atom induced the adsorption of another O at the adjacent equivalent hollow site  
9 of the Cu terrace results in the spontaneous detachment of the Cu atom (marked by the white dashed circle)  
10 from the step edge. (d) The continued O adsorption at the equivalent hollow sites along the step edge  
11 results in the extension of the Cu terrace. (e) PODS of Cu 3d and Au 5d for the pristine step in (a). (f) PODS  
12 of Cu 3d, Au 5d, and O 2p of the step with an adsorbed O atom in (b). (g) O adsorbs at the bridge site  
13 consisting of three coordinating Cu atoms and two coordinating Au atoms, destabilizing the adjacent Au  
14 atom (marked by the white dashed circle). (h) The departure of the Au atom in the CuAu terrace results in  
15 the spontaneous detachment of the Cu atoms (marked by the white dashed circles). (i) The departure of  
16 the two Cu atoms results in the formation of two [110] steps (marked with the red rectangles) that are similar  
17 to the step configuration in (a), where the two four-fold hollow sites (marked by red dashed circles) are  
18 subjected to O adsorption to form the c(2×2)-O structure.

19

1 We then examine O-adsorption induced pit formation in the CuAu terrace. Fig. 9(g) shows  
2 the CuAu terrace, in which the four-fold hollow site is found to be more favorable than the  
3 neighboring bridge site for O adsorption. The presence of adsorbed O at the hollow site promotes  
4 the abstraction of the adjacent Au from the terrace, as marked by the white dashed circle in Fig.  
5 9(g). This is shown by the change in the vacancy formation energies of the Au atom, which are  
6 calculated to be 0.94 eV and 0.56 eV before and after the O adsorption. Upon the abstraction of  
7 the Au atom, the adjacent Cu atoms as marked by the white dashed circle in Fig. 9(h) become  
8 undercoordinated, and their small vacancy formation (0.24 eV) makes these Cu atoms readily  
9 detach from the surface at the elevated temperature of the experiment. The O adsorption induced  
10 departure of the Au and Cu atoms results in a monolayer pit in the CuAu terrace and thus exposes  
11 the underlying Cu plane. As marked by the red solid rectangles in Fig. 9(i), the Cu-Au-Cu rows  
12 adjacent to the surface pit locally have the same step-terrace configuration as that in Fig. 9(b),  
13 and the hollow sites marked with the red dashed circles have five coordinating Cu atoms and thus  
14 are more favorable for O adsorption. In the same manner as shown in Figs. 9(b-d), O adsorption  
15 at these hollow sites of the exposed Cu plane significantly destabilizes the Au and Cu atoms along  
16 the step edge. The continued O adsorption results in the exfoliation of the CuAu layer along with  
17 the nucleation and growth of the  $c(2 \times 2)$ -O on the exposed Cu plane, as shown in our STM images  
18 (Figs. 2-5). As also shown from our STM observations, the  $\text{Cu}_3\text{Au}(100)$  consists of a high density  
19 of steps and terraces, and oxygen adsorption induced decomposition of the topmost CuAu layer  
20 tends to happen more readily from the steps. This is consistent with DFT calculations, showing  
21 that the CuAu decomposition from the terraces requires a larger energy barrier than that at steps.

22

## 23 **4. Discussion**

1 Cu-Au was studied as a simplest-possible binary alloy system (only one of the  
2 components oxidizes) for understanding the effect of the noble metal addition on the initial-stage  
3 oxidation of alloys [14,15,19,35,36,38,42–44]. For the Cu<sub>3</sub>Au(100), it was shown that O atoms  
4 preferentially adsorb at the four-fold hollow sites of the Cu-terminated surface (including the  
5 segregation of impurity O in the Cu<sub>3</sub>Au bulk to the hollow sites of the (100) surface [31]) with no  
6 Au detected in the first layer [26,31,53,45–52]. However, the microscopic mechanism for the O  
7 adsorption induced formation of the Cu-terminated surface has not been identified. On one hand,  
8 our results have shown that the O<sub>2</sub> exposure results in the Cu-terminated,  $c(2\times 2)$ -O surface, which  
9 is consistent with previous studies. On the other hand, our results provide new insight into the  
10 microscopic process underlying the formation of the Cu-terminated surface. Counterintuitive to  
11 the common expectations of the adsorbate-induced surface segregation of the more reactive alloy  
12 component [33,46,53–56], our observations demonstrate that the formation of the Cu surface  
13 termination occurs via the O adsorption induced decomposition (de-alloying) of the topmost CuAu  
14 surface layer. As shown from the STM imaging and LEED (Fig. 1), the pristine Cu<sub>3</sub>Au(100) surface  
15 is dominated by CuAu-terminated terraces separated by monatomic steps and narrow Cu-  
16 terminated terraces. The O<sub>2</sub> exposure results in the O adsorption induced decomposition of the  
17 CuAu terraces via the receding motion of the existing atomic steps as well as the nucleation of  
18 monolayer depressions in the CuAu terraces and their subsequent growth induced by the  
19 retraction motion of the resultant monatomic steps. This is similar to the exfoliation that leads to  
20 the peeling off of the outermost CuAu layer, thereby exposing the inner Cu plane to the O attack.

21 The O adsorption induced decomposition of the topmost surface layer is similar to a  
22 chemical peeling procedure in which a chemical solution is applied to the surface to remove the  
23 top layers. This chemical peeling bears a clear difference from the O adsorption induced surface  
24 segregation although both result in a Cu-terminated Cu surface. The O-adsorption induced

1 surface segregation requires counter diffusion of Au and Cu atoms between the surface and  
2 subsurface regions. That is, the surface segregation of Cu atoms from the subsurface layer is  
3 accompanied with the inward diffusion of Au atoms in the topmost layer, for which Cu is depleted  
4 from the inner layers whereas Au is enriched in the subsurface. By contrast, the O-adsorption  
5 induced surface peeling process itself does not require the mass exchanges between the surface  
6 and subsurface because it only involves the topmost layer, which therefore does not induce  
7 significant composition changes to the subsurface region. This is confirmed by our STM imaging  
8 (Figs. 2-5), showing the formation of Cu clusters via the aggregation of Cu adatoms supplied from  
9 the decomposing CuAu surface layer and dissolution of resulting Au adatoms into the subsurface  
10 of the  $\text{Cu}_3\text{Au}$  crystal. The latter is corroborated by the depth-resolved AP-XPS and LEIS  
11 measurements (Figs. 6, 7), showing the absence of Au in the surface but enrichment of Au in the  
12 subsurface region during the  $\text{O}_2$  exposure.

13         These fundamental insights may have practical implications. As shown above, the  $\text{Cu}_3\text{Au}$   
14 surface can easily decompose into Cu and Au adatoms with the low  $\text{O}_2$  pressure, and the Cu  
15 adatoms subsequently aggregate into clusters along the dissolution of Au adatoms into the bulk.  
16 The Cu clusters may be oxidized into  $\text{CuO}_x$  islands upon the continued  $\text{O}_2$  exposure or with a  
17 higher oxygen chemical potential, which may serve as oxide nuclei for further oxidation. This is in  
18 line with the in-situ electron microscopy observations showing the formation of  $\text{Cu}_2\text{O}$  islands from  
19 the Cu-Au oxidation at the higher  $\text{O}_2$  pressure and temperature [57–61]. As oxidation continues,  
20 particularly at large  $\text{O}_2$  pressures, oxide islands impinge and result in interfaces (grain boundaries)  
21 in the oxide film, which may serve as short-circuit diffusion paths for outward diffusion of Cu atoms  
22 or inward diffusion of O atoms and thus lead to the poor oxidation resistance. Therefore, a control  
23 in the density of the Cu clusters in the very early stages of the oxidation may provide a control  
24 over the nucleation density of the oxide islands and thus the microstructure feature of the oxide

1 film. As shown in Figs. 2-5, the longer O<sub>2</sub> annealing can significantly reduce the surface density  
2 of Cu clusters. It is reasonable to expect for the further reduction in the number density of Cu  
3 clusters with a higher annealing temperature to enhance the surface diffusion of Cu adatoms.

4 Another case is heterogeneous catalysis that utilizes Cu and Cu alloys as catalysts for  
5 various catalytic oxidation reactions. For instance, bimetallic Cu-Au alloys have attracted  
6 considerable attention recently as an improved catalyst in CO oxidation [2], propene  
7 epoxidation [62] and benzyl alcohol oxidation [63]. These catalytic reactions initiate from the  
8 surface oxidation of the alloy, where the catalytic activity depends on the surface termination,  
9 composition, atomic structure, and morphology. As shown from our experiments and modeling,  
10 the O<sub>2</sub> exposure results in the decomposition of the CuAu terminated surface layer into a large  
11 number of single adatoms of Cu and Au (before dissolving into the bulk for the latter) and their  
12 clusters along with the O adsorption into the four-fold hollow sites of the Cu terminated surface  
13 layer. Our results indicate that relative surface densities of these atomic species and their  
14 clustering behavior can be controlled by O<sub>2</sub> annealing conditions such as temperature and oxygen  
15 pressure. The interplay among these single adatoms, their clusters, and chemisorbed O may play  
16 an important role in influencing the dynamic evolution of the catalytic performance. Further  
17 investigations are needed to elucidate such interplay.

## 18

## 19 **5. Conclusions**

20 The microscopic process underlying the initial-stage oxidation of Cu<sub>3</sub>Au(100) has been  
21 investigated using a combination of surface science tools and atomistic modeling. The pristine  
22 surface consists of wide CuAu terraces and narrow Cu terraces separated by monatomic steps.  
23 The oxygen exposure induces decomposition (de-alloying) of the topmost CuAu layer via the  
24 receding motion of atomic steps and nucleation/growth of monolayer pits in CuAu terraces, which

1 results in a large number of Cu adatoms aggregating into Cu clusters and Au adatoms dissolving  
2 into the bulk. This O-adsorption induced “peeling off” of the CuAu layer exposes the underlying  
3 Cu plane to the O attack. The O adsorption into the four-fold hollow sites of the exposed Cu plane  
4 results in the nucleation and growth of the  $c(2\times 2)$ -O superstructure, which can be fit well by the  
5 JMAK theory with a site-saturate nucleation. We expect that the present results may also be  
6 relevant to the behavior of other alloys composed of both reactive and noble components, for  
7 which the dramatic difference of the chemical reactivity of the alloying elements may drive the de-  
8 alloying at the surface.

9

10 **Acknowledgement**

11 This work was supported by the U.S. Department of Energy, Office of Basic Energy Sciences,  
12 Division of Materials Sciences and Engineering under Award No. DE-SC0001135. The authors  
13 thank N.P. Guisinger at Argonne National Laboratory for help with the STM experiments. Use of  
14 the Center for Nanoscale Materials, an Office of Science user facility, was supported by the U.S.  
15 Department of Energy, Office of Science, Office of Basic Energy Sciences, under Contract No.  
16 DE-AC02-06CH11357. This research also used resources of the Center for Functional  
17 Nanomaterials, and the Scientific Data and Computing Center, a component of the Computational  
18 Science Initiative, and the National Synchrotron Light Source II, which are U.S. DOE Office of  
19 Science Facilities, at Brookhaven National Laboratory under Contract No. DE-SC0012704. This  
20 work used the computational resources from the Extreme Science and Engineering Discovery  
21 Environment (XSEDE), which is supported by National Science Foundation grant number OCI-  
22 1053575.

23

24

25

26

## 1   **References**

2  
3  
4  
5  
6  
7  
8  
9  
10  
11  
12  
13  
14  
15  
16  
17  
18  
19  
20  
21  
22

[1] C. Bracey, P. Ellis, and G. Hutchings, *Application of Copper–Gold Alloys in Catalysis: Current Status and Future Perspectives*, Chem. Soc. Rev. **38**, 2231 (2009).

[2] S. Najafishirtari, R. Brescia, P. Guardia, S. Marras, L. Manna, and M. Colombo, *Nanoscale Transformations of Alumina-Supported AuCu Ordered Phase Nanocrystals and Their Activity in CO Oxidation*, ACS Catal. **5**, 2154 (2015).

[3] L. Luo, S. Chen, Q. Xu, Y. He, Z. Dong, L. Zhang, J. Zhu, Y. Du, B. Yang, and C. Wang, *Dynamic Atom Clusters on AuCu Nanoparticle Surface during CO Oxidation*, J. Am. Chem. Soc. **142**, 4022 (2020).

[4] E. Andrews, Y. Fang, and J. Flake, *Electrochemical Reduction of CO<sub>2</sub> at CuAu Nanoparticles: Size and Alloy Effects*, J. Appl. Electrochem. **48**, 435 (2018).

[5] Y. Xiao, L. Tang, W. Zhang, and C. Shen, *Theoretical Insights into the Selective and Activity of CuAu Catalyst for O<sub>2</sub> and CO<sub>2</sub> Electroreduction*, Comput. Mater. Sci. **192**, 110402 (2021).

[6] H. Iwai, T. Umeki, M. Yokomatsu, and C. Egawa, *Methanol Partial Oxidation on Cu-Zn Thin Films Grown on Ni(1 0 0) Surface*, Surf. Sci. **602**, 2541 (2008).

[7] P. Mierczynski, K. Vasilev, A. Mierczynska, W. Maniukiewicz, R. Ciesielski, J. Rogowski, I. M. Szykowska, A. Y. Trifonov, S. V. Dubkov, D. G.

1 Gromov, and T. P. Maniecki, *The Effect of Gold on Modern Bimetallic Au-*  
2 *Cu/MWCNT Catalysts for the Oxy-Steam Reforming of Methanol*, Catal. Sci.  
3 Technol. **6**, 4168 (2016).

4 [8] J. A. Rodriguez, P. Liu, J. Hrbek, J. Evans, and M. Pérez, *Water Gas Shift*  
5 *Reaction on Cu and Au Nanoparticles Supported on CeO<sub>2</sub>(111) and ZnO(0001):*  
6 *Intrinsic Activity and Importance of Support Interactions*, Angew. Chemie - Int. Ed.  
7 **46**, 1329 (2007).

8 [9] S. Xia, L. Fang, Y. Meng, X. Zhang, L. Zhang, C. Yang, and Z. Ni, *Water-*  
9 *Gas Shift Reaction Catalyzed by Layered Double Hydroxides Supported Au-*  
10 *Ni/Cu/Pt Bimetallic Alloys*, Appl. Catal. B Environ. **272**, 118949 (2020).

11 [10] C. Li, P. Zhang, J. Wang, J. A. Boscoboinik, and G. Zhou, *Tuning*  
12 *the Deoxygenation of Bulk-Dissolved Oxygen in Copper*, J. Phys. Chem. C **122**,  
13 8254 (2018).

14 [11] J. Wang, D. Lu, C. Li, Y. Zhu, J. A. Boscoboinik, and G. Zhou,  
15 *Measuring Charge Transfer between Adsorbate and Metal Surfaces*, J. Phys.  
16 Chem. Lett. **11**, 6827 (2020).

17 [12] C. Li, Q. Liu, J. A. Boscoboinik, and G. Zhou, *Tuning the Surface*  
18 *Composition of Cu<sub>3</sub>Au Binary Alloy*, Phys. Chem. Chem. Phys. **22**, 3379 (2020).

19 [13] J. Wang, C. Li, Y. Zhu, J. A. Boscoboinik, and G. Zhou, *Insight into*  
20 *the Phase Transformation Pathways of Copper Oxidation: From Oxygen*  
21 *Chemisorption on the Clean Surface to Multilayer Bulk Oxide Growth*, J. Phys.  
22 Chem. C **122**, 26519 (2018).

- 1 [14] M. Kittel, M. Polcik, R. Terborg, J. T. Hoeft, P. Baumgärtel, A. M.  
2 Bradshaw, R. L. Toomes, J. H. Kang, D. P. Woodruff, M. Pascal, C. L. A. Lamont,  
3 and E. Rotenberg, *Structure of Oxygen on Cu(1 0 0) at Low and High Coverages*,  
4 *Surf. Sci.* **470**, 311 (2001).
- 5 [15] G. Kresse and J. Hafner, *Ab Initio Molecular Dynamics for Liquid*  
6 *Metals*, *Phys. Rev. B* **47**, 558 (1993).
- 7 [16] G. Kresse, J. Furthmüller, and J. Hafner, *Theory of the Crystal*  
8 *Structures of Selenium and Tellurium: The Effect of Generalized-Gradient*  
9 *Corrections to the Local-Density Approximation*, *Phys. Rev. B* **50**, 13181 (1994).
- 10 [17] G. Kresse and J. Furthmüller, *Efficiency of Ab-Initio Total Energy*  
11 *Calculations for Metals and Semiconductors Using a Plane-Wave Basis Set*,  
12 *Comput. Mater. Sci.* **6**, 15 (1996).
- 13 [18] D. Joubert, *From Ultrasoft Pseudopotentials to the Projector*  
14 *Augmented-Wave Method*, *Phys. Rev. B - Condens. Matter Mater. Phys.* **59**, 1758  
15 (1999).
- 16 [19] J. P. Perdew, J. A. Chevary, S. H. Vosko, K. A. Jackson, M. R.  
17 Pederson, D. J. Singh, and C. Fiolhais, *Erratum: Atoms, Molecules, Solids, and*  
18 *Surfaces: Applications of the Generalized Gradient Approximation for Exchange*  
19 *and Correlation (Physical Review B (1993) 48, 7, (4978))*, *Phys. Rev. B* **48**, 4978  
20 (1993).

- 1 [20] J. Li, S. Zhang, C. Li, Y. Zhu, J. A. Boscoboinik, X. Tong, J. T.  
2 Sadowski, G. Wang, and G. Zhou, *Coupling between Bulk Thermal Defects and*  
3 *Surface Segregation Dynamics*, Phys. Rev. B **104**, 16 (2021).
- 4 [21] K. Hu, M. Wu, S. Hinokuma, T. Ohto, M. Wakisaka, J. I. Fujita, and  
5 Y. Ito, *Boosting Electrochemical Water Splitting: Via Ternary NiMoCo Hybrid*  
6 *Nanowire Arrays*, J. Mater. Chem. A **7**, 2156 (2019).
- 7 [22] L. Houssiau and P. Bertrand, *Direct Observation of the Rippling*  
8 *and the Order-Disorder Transition at the Cu<sub>3</sub>Au(100) Surface by TOF-Ion*  
9 *Scattering*, Surf. Sci. **352–354**, 978 (1996).
- 10 [23] S. Terreni, M. Canepa, L. Mattera, and V. A. Esaulov, *The*  
11 *Structure of the Cu<sub>3</sub>Au(0 0 1) Surface Studied by Impact Collision of Low Energy*  
12 *Ne Ions*, Nucl. Instr. and Meth. in Phys. Res. B. **193**, 550 (2002).
- 13 [24] W. E. Wallace and G. J. Ackland, *Calculated Energies and*  
14 *Relaxations of the Low-Index Planes of Ordered Cu<sub>3</sub>Au*, Surf. Sci. **275**, (1992).
- 15 [25] Z. Q. Wang, Y. S. Li, C. K. C. Lok, J. Quinn, F. Jona, and P. M.  
16 Marcus, *Atomic and Electronic Structure of a Surface Alloy - Comparison with the*  
17 *Bulk Alloy*, Solid State Communications. **62**, 181 (1987).
- 18 [26] H. Niehus and C. Achete, *Surface Structure Investigation of*  
19 *Nitrogen and Oxygen on Cu<sub>3</sub>Au(100)*, Surf. Sci. **289**, 19 (1993).
- 20 [27] C. Mannori, T. Scimia, P. Cantini, S. Terreni, M. Canepa, and L.  
21 Mattera, *The Cu<sub>3</sub>Au(001) Surface: A He Diffraction Study*, Surf. Sci. **433–435**,  
22 307 (1999).

- 1 [28] F. Wang, J. M. Zhang, Y. Zhang, and V. Ji, *Structural Properties*  
2 *and Diffusion Processes of the Cu<sub>3</sub>Au (0 0 1) Surface*, Appl. Surf. Sci. **256**, 7083  
3 (2010).
- 4 [29] T. Fujita, Y. Okawa, Y. Matsumoto, and K. ichi Tanaka, *Phase*  
5 *Boundaries of Nanometer Scale c(2x2)-O Domains on the Cu(100) Surface*,  
6 Phys. Rev. B - Condens. Matter Mater. Phys. **54**, 2167 (1996).
- 7 [30] H. Iddir, D. D. Fong, P. Zapol, P. H. Fuoss, L. A. Curtiss, G. W.  
8 Zhou, and J. A. Eastman, *Order-Disorder Phase Transition of the Cu(001)*  
9 *Surface under Equilibrium Oxygen Pressure*, Phys. Rev. B - Condens. Matter  
10 Mater. Phys. **76**, 2 (2007).
- 11 [31] A. A. Leitão, L. G. Dias, M. Dionízio Moreira, F. Stavale, H. Niehus,  
12 C. A. Achete, and R. B. Capaz, *Signatures of Oxygen on Cu<sub>3</sub>Au (100): From*  
13 *Isolated Impurity to Oxide Regimes*, Phys. Rev. B - Condens. Matter Mater. Phys.  
14 **82**, 2 (2010).
- 15 [32] K. Oka, Y. Tsuda, T. Makino, M. Okada, M. Hashinokuchi, A.  
16 Yoshigoe, Y. Teraoka, and H. Kasai, *The Effects of Alloying and Segregation for*  
17 *the Reactivity and Diffusion of Oxygen on Cu<sub>3</sub>Au(111)*, Phys. Chem. Chem. Phys.  
18 **16**, 19702 (2014).
- 19 [33] M. Okada, Y. Tsuda, K. Oka, K. Kojima, W. A. Diño, A. Yoshigoe,  
20 and H. Kasai, *Experimental and Theoretical Studies on Oxidation of Cu-Au Alloy*  
21 *Surfaces: Effect of Bulk Au Concentration*, Sci. Rep. **6**, 1 (2016).

- 1 [34] W. A. Saidi, M. Lee, L. Li, G. Zhou, and A. J. H. McGaughey, *Ab*  
2 *Initio Atomistic Thermodynamics Study of the Early Stages of Cu(100) Oxidation*,  
3 Phys. Rev. B - Condens. Matter Mater. Phys. **86**, 1 (2012).
- 4 [35] M. Lee and A. J. H. McGaughey, *Energetics and Kinetics of the*  
5 *c(2×2) to (2√2×√2) R45° Transition during the Early Stages of Cu(100) Oxidation*,  
6 Phys. Rev. B - Condens. Matter Mater. Phys. **83**, 1 (2011).
- 7 [36] A. Posada-Borbón, B. Hagman, A. Schaefer, C. Zhang, M. Shipilin,  
8 A. Hellman, J. Gustafson, and H. Grönbeck, *Initial Oxidation of Cu(100) Studied*  
9 *by X-Ray Photo-Electron Spectroscopy and Density Functional Theory*  
10 *Calculations*, Surf. Sci. **675**, 64 (2018).
- 11 [37] H. H. Brongersma, M. Carrere-Fontaine, R. Cortenraad, A. W.  
12 Denier Van Der Gon, P. J. Scanlon, I. Spolveri, B. Cortigiani, U. Bardi, E.  
13 Taglauer, S. Reiter, S. Labich, P. Bertrand, L. Houssiau, S. Speller, S.  
14 Parascandola, H. Ünlü-Lachnitt, and W. Heiland, *A Round Robin Experiment of*  
15 *Elemental Sensitivity Factors in Low-Energy Ion Scattering*, Nucl. Instr. and Meth.  
16 in Phys. Res. B. **142**, 377 (1998).
- 17 [38] D. Wu, Q. Liu, J. Li, J. T. Sadowski, and G. Zhou, *Visualizing*  
18 *Reversible Two-Dimensional Phase Transitions in Oxygen Chemisorbed Layers*,  
19 J. Phys. Chem. C **122**, 28233 (2018).
- 20 [39] D. Wu, J. Li, and G. Zhou, *Oxygen Adsorption at Heterophase*  
21 *Boundaries of the Oxygenated Cu(110)*, Surf. Sci. **666**, 28 (2017).

- 1 [40] W. A. J. and R. Mehl, *Reaction Kinetics in Processes of Nucleation*  
2 *and Growth*. Trans. Am. Inst. Min Metall. Eng, **135**, 416 (1939).
- 3 [41] M. Fanfoni and M. Tomellini, *The Johnson-Mehl-Avrami-*  
4 *Kolmogorov Model: A Brief Review*, Nuovo Cim. Della Soc. Ital. Di Fis. D -  
5 Condens. Matter, At. Mol. Chem. Physics, Biophys. **20**, 1171 (1998).
- 6 [42] X. Wang, J. C. Hanson, A. I. Frenkel, J. Y. Kim, and J. A.  
7 Rodriguez, *Time-Resolved Studies for the Mechanism of Reduction of Copper*  
8 *Oxides with Carbon Monoxide: Complex Behavior of Lattice Oxygen and the*  
9 *Formation of Suboxides*, J. Phys. Chem. B **108**, 13667 (2004).
- 10 [43] A. Wilson, R. Bernard, Y. Borensztein, B. Croset, H. Cruguel, A.  
11 Vlad, A. Coati, Y. Garreau, and G. Prévot, *Critical Au Concentration for the*  
12 *Stabilization of Au-Cu Nanoparticles on Rutile against Dissociation under Oxygen*,  
13 J. Phys. Chem. Lett. **6**, 2050 (2015).
- 14 [44] Q. Liu, Y. Ning, W. Huang, Q. Fu, F. Yang, and X. Bao, *Origin of*  
15 *the Thickness-Dependent Oxidation of Ultrathin Cu Films on Au(111)*, J. Phys.  
16 Chem. C **122**, 8364 (2018).
- 17 [45] A. A. Leitão, M. D. Moreira, L. G. Dias, A. M. Silva, R. B. Capaz,  
18 and C. A. Achete, *Ab Initio Studies of Pristine and Oxidized Cu<sub>3</sub>Au(100) and*  
19 *(111) Surfaces*, J. Mater. Sci. **47**, 7594 (2012).
- 20 [46] O. Bauer, C. H. Schmitz, J. Ikononov, M. Willenbockel, S.  
21 Soubatch, F. S. Tautz, and M. Sokolowski, *Au Enrichment and Vertical Relaxation*

- 1        *of the Cu<sub>3</sub>Au(111) Surface Studied by Normal-Incidence x-Ray Standing Waves*,  
2        Phys. Rev. B **93**, 1 (2016).
- 3        [47]        G. K. Wertheim, L. F. Mattheiss, and D. N. E. Buchanan, *Partial*  
4        *Densities of States of Ordered Cu<sub>3</sub>Au*, Phys. Rev. B **38**, 5988 (1988).
- 5        [48]        M. T. Lin, J. Shen, W. Kuch, H. Jenniches, M. Klaua, C. M.  
6        Schneider, and J. Kirschner, *Growth, Morphology, and Crystalline Structure of*  
7        *Ultrathin Fe Films on Cu<sub>3</sub>Au(100)*, Surf. Sci. **410**, 290 (1998).
- 8        [49]        G. C. S. Valadares, F. M. T. Mendes, M. Dionízio Moreira, A. A.  
9        Leitão, H. Niehus, R. B. Capaz, and C. A. Achete, *Structural Determination of*  
10        *Stable MoO<sub>x</sub> Monolayers on O/Cu<sub>3</sub>Au(1 0 0): DFT Calculations*, Chem. Phys.  
11        **406**, 47 (2012).
- 12        [50]        M. Hashinokuchi, A. Yoshigoe, Y. Teraoka, and M. Okada,  
13        *Temperature Dependence of Cu<sub>2</sub>O Formation on Cu<sub>3</sub>Au(110) Surface with*  
14        *Energetic O<sub>2</sub> Molecular Beams*, Appl. Surf. Sci. **287**, 282 (2013).
- 15        [51]        A. M. Silva, C. A. Achete, and R. B. Capaz, *First-Principles Study of*  
16        *Oxygen-Induced Copper Segregation in Cu<sub>3</sub>Au(1 1 1)*, Chem. Phys. **410**, 99  
17        (2013).
- 18        [52]        F. U. Renner, G. A. Eckstein, L. Lymperakis, A. Dakkouri-Baldauf,  
19        M. Rohwerder, J. Neugebauer, and M. Stratmann, *In Situ Scanning Tunneling*  
20        *Microscopy Study of Selective Dissolution of Au<sub>3</sub>Cu and Cu<sub>3</sub>Au (0 0 1)*,  
21        Electrochim. Acta **56**, 1694 (2011).

- 1 [53] R. F. Shannon, S. E. Nagler, C. R. Harkless, and R. M. Nicklow,  
2 *Time-Resolved x-Ray-Scattering Study of Ordering Kinetics in Bulk Single-Crystal*  
3 *Cu<sub>3</sub>Au*, Phys. Rev. B **46**, 40 (1992).
- 4 [54] Y. Huang and J. M. Cowley, *A Study of the Cu<sub>3</sub>Au(110) Surface*  
5 *Structure by RHEED*, Surf. Sci. **285**, 42 (1993).
- 6 [55] M. Okada, M. Hashinokuchi, M. Fukuoka, T. Kasai, K. Moritani, and  
7 Y. Teraoka, *Protective Layer Formation during Oxidation of Cu<sub>3</sub>Au(100) Using*  
8 *Hyperthermal O<sub>2</sub> Molecular Beam*, Appl. Phys. Lett. **89**, 17 (2006).
- 9 [56] M. Dionízio Moreira, G. N. Fontes, H. Niehus, C. A. Achete, and R.  
10 B. Capaz, *First-Principles Calculations and XPS Measurements of Gold*  
11 *Segregation at the Cu<sub>3</sub>Au(111) Surface*, J. Vac. Sci. Technol. B, Nanotechnol.  
12 Microelectron. Mater. Process. Meas. Phenom. **30**, 051802 (2012).
- 13 [57] G. W. Zhou, J. A. Eastman, R. C. Birtcher, P. M. Baldo, J. E.  
14 Pearson, L. J. Thompson, L. Wang, and J. C. Yang, *Composition Effects on the*  
15 *Early-Stage Oxidation Kinetics of (001) Cu-Au Alloys*, J. Appl. Phys. **101**, 3  
16 (2007).
- 17 [58] L. Luo, Y. Kang, J. C. Yang, and G. Zhou, *Effect of Gold*  
18 *Composition on the Orientations of Oxide Nuclei during the Early Stage Oxidation*  
19 *of Cu-Au Alloys*, J. Appl. Phys. **111**, (2012).
- 20 [59] L. Luo, Y. Kang, J. C. Yang, D. Su, E. A. Stach, and G. Zhou,  
21 *Comparative Study of the Alloying Effect on the Initial Oxidation of Cu-Au(100)*  
22 *and Cu-Pt(100)*, Appl. Phys. Lett. **104**, (2014).

- 1 [60] G. W. Zhou, L. Wang, R. C. Birtcher, P. M. Baldo, J. E. Pearson, J.  
2 C. Yang, and J. A. Eastman, *Cu<sub>2</sub>O Island Shape Transition during Cu-Au Alloy*  
3 *Oxidation*, Phys. Rev. Lett. **96**, 2 (2006).
- 4 [61] L. Luo, Y. Kang, Z. Liu, J. C. Yang, and G. Zhou, *Effect of Oxygen*  
5 *Pressure on the Initial Oxidation Behavior of Cu and Cu-Au Alloys*, Mater. Res.  
6 Soc. Symp. Proc. **1318**, 31 (2011).
- 7 [62] R. J. Chimentão, F. Medina, J. L. G. Fierro, J. Llorca, J. E. Sueiras,  
8 Y. Cesteros, and P. Salagre, *Propene Epoxidation by Nitrous Oxide over Au-*  
9 *Cu/TiO<sub>2</sub> Alloy Catalysts*, J. Mol. Catal. A Chem. **274**, 159 (2007).
- 10 [63] C. Della Pina, E. Falletta, and M. Rossi, *Highly Selective Oxidation*  
11 *of Benzyl Alcohol to Benzaldehyde Catalyzed by Bimetallic Gold-Copper Catalyst*,  
12 J. Catal. **260**, 384 (2008).  
13